Progress of Theoretical Physics, Vol. 114, No. 4, October 2005

# Generalized Dynamical Ordering and Topological Entropy in the Hénon Map

Yoshihiro YAMAGUCHI[1] and Kiyotaka TANIKAWA[2]

[1] *Teikyo Heisei University, Ichihara 290-0193, Japan*
[2] *National Astronomical Observatory, Mitaka 181-8588, Japan*

(Received May 11, 2005)

Under area- and orientation-preserving maps, the images of the symmetry axes accumulate at the unstable manifold of a saddle fixed point $P$, while their inverse images accumulate at the stable manifold of $P$. Before or after the tangency of these stable and unstable manifolds, four types of generalized dynamical ordering are derived. They determine the order of the appearance of the symmetric periodic orbits. We derive these types of ordering for the area- and orientation-preserving Hénon map. A lower bound of the topological entropy is obtained by using the symbol sequence of the periodic orbits included in the dynamical ordering and the trellis method.

## §1. Introduction

The tangency of the stable and unstable manifolds of a saddle fixed point or a periodic point gives rise to rich phenomena[1)] related to the change of complexity in a given system. We are particularly interested in tangency in the case of reversible area- and orientation-preserving maps. If such a map can be expressed as a product of two involutions,[2)] then it is said to be reversible, and it possesses symmetry axes.[3)] The forward images of these symmetry axes accumulate at the unstable manifold of a saddle fixed point, and their inverse images accumulate at the stable manifold. As a result, before or after tangency, infinitely many symmetric periodic orbits appear through saddle-node or equi-period bifurcations. For these periodic orbits, the dynamical ordering (DO) is determined. This DO is represented by two-dimensional order relations.[4),5)] Using information with respect to the periodic orbits included in the DO, we determine a lower bound of the topological entropy $h_{\rm top}$.[6),7)] The DO gives useful information concerning the complexity before and after the tangency of the stable and unstable manifolds. We call this method of analyzing the complexity of a system the dynamical ordering method (DOM).

The trellis method developed by Collins[8)] is a powerful method for obtaining a lower bound of the topological entropy $h_{\rm top}$. This method uses a trellis, which is a finite portion of the tangle of stable and unstable manifolds of a saddle fixed point. In order to calculate $h_{\rm top}$, we consider the condition of tangency, because the construction of a compatible graph for the trellis in this case is easier than in the case of intersection. Another useful method is the braid method, i.e. the method employing the symbol sequence for periodic orbits included in the DO. When using the braid or symbol sequence method to calculate $h_{\rm top}$, the software *Wintrain*, developed by Hall,[9)] is helpful.

The above mentioned methods are all based on the Nielsen-Thurston theorem (NT).[10)−12)] The train track method (TTM) is an algorithmic proof of NT.[13)] A proof of the validity of the trellis method was obtained using the TTM. After constructing the compatible graph in the TTM or constructing the braid (symbol sequence) in the DOM, the transition matrix $M$ is determined, and the largest eigenvalue $\lambda_{\max}$ of $M$ is evaluated.[7),13)] Thus, a lower bound of the topological entropy is obtained as $h_{\rm top} \geq \ln \lambda_{\max}$.

In the present paper, we derive a family of dynamical orderings for the area- and orientation-preserving Hénon map.[14)] Then, we apply the trellis method and the DOM for the Hénon map to calculate $h_{\rm top}$. The original area- and orientation-preserving Hénon map $T_{\rm H}$ is defined in the $(x, y)$-plane as

$$y_{n+1} = x_n + 1 - \tilde{a} y_n^2, \tag{1}$$

$$x_{n+1} = -y_n, \tag{2}$$

where $\tilde{a} > 0$ is a parameter. After a coordinate change and a scale transformation, $T_{\rm H}$ can be rewritten in the following form $T$:

$$y_{n+1} = y_n + f(x_n), \tag{3}$$

$$x_{n+1} = x_n + y_{n+1}. \tag{4}$$

Here, $f(x) = a(x - x^2)$ and $a > 0$ is a parameter. There exist two fixed points, $P = (0, 0)$ and $Q = (1, 0)$, where $P$ is a saddle and $Q$ is an elliptic point (for $0 < a < 4$) or a saddle with a reflection (for $a > 4$). At $a = 4$, a period-doubling bifurcation of $Q$ occurs. The above symplectic form is useful for understanding the structure of the stable and unstable manifolds of $P$ and of the symmetry axes. We study the Hénon map using the form given in Eqs. (3) and (4).

With the aid of the numerical method developed by Biham and Wenzel,[15),16)] the number of periodic points has been obtained.[17),18)] Here let $q_{\max}$ be the maximum period and $N_{q_{\max}}(a)$ be the total number of periodic points of period $q$, satisfying $1 \leq q \leq q_{\max}$, at a fixed value of $a$. The value of $q_{\max}$ was found to be 20 in Refs. 17) and 24) in Ref. 18). It has been shown that the function $N_{q_{\max}}(a)$ has interesting properties. For example, $N_{q_{\max}}(a)$ is a monotonic function of $a$. In addition, $N_{q_{\max}}(a)$ seems to have infinitely many plateaus. These facts suggest that the lower bound of the topological entropy $h_{\rm top}$ may be a monotonic function of $a$, and it may be constant in the plateau regions. In order to establish these properties, the pruning theory and an algorithm for pruning have been proposed.[19)]

The two ends of a plateau correspond to certain tangency conditions of the stable and unstable manifolds of $P$. The arcs of the stable and unstable manifolds forming the tangency that determines the beginning of the plateau are not necessarily those forming the tangency that determines the end. We can apply the trellis method to calculate $h_{\rm top}$ at the two ends of a plateau and apply the DOM for the parameter regions in the vicinities of both the ends.

Hereafter, let $a_{\rm hs}$ be the critical value at which the horseshoe for $T$ is completed. The numerical value of $a_{\rm hs}$ is $5.1766\cdots$. The topological entropy $h_{\rm top}$ and $N_{q_{\max}}(a)$ have been extensively calculated in the vicinity of $a_{\rm hs}$, and many plateaus in the

graphs of $N_{q_{\max}}(a)$ and $h_{\rm top}(a)$ have been found in this parameter region.[17)–19)] We give a detailed study of this parameter region in §4. In the region $3.242 < a < 4.045$, there exists the largest plateau in the graph of $N_{q_{\max}}(a)$.[18)] We study this region in §5.

In §2, we prepare the basic tools used in later sections. We derive four types of the dynamical ordering in §3. Using both the trellis method and DOM, a lower bound of the topological entropy is obtained in §§4 and 5. In §6, we discuss on some implications of the plateaus of the entropy function.

## §2. Basic tools

### 2.1. *Symmetry axes and homoclinic lobes*

The Hénon map $T$ is reversible; that is, it can be expressed as a product of two involutions $h$ and $g$ as

$$T = h \circ g, \tag{5}$$

where $h$ and $g$ are defined by

$$g\begin{pmatrix} x \\ y \end{pmatrix} = \begin{pmatrix} x \\ -y - f(x) \end{pmatrix} \tag{6}$$

and

$$h\begin{pmatrix} x \\ y \end{pmatrix} = \begin{pmatrix} x - y \\ -y \end{pmatrix}, \tag{7}$$

with $\det\nabla h = \det\nabla g = -1$. The sets of fixed points of $h$ and $g$ are called the symmetry axes.[3)] We refer to them as $S_1$ and $S_2$ for $h$ and $g$, respectively:

$$S_1 = \{(x, y) : y = 0\}, \tag{8}$$

$$S_2 = \{(x, y) : y = -f(x)/2\}. \tag{9}$$

Let $W_u = W_u(P)$ be the branch of the unstable manifold starting at $P$ and extending in the upper-right direction and $W_s = W_s(P)$ be that of the stable manifold extending in the lower-right direction. We explain the relation between the stable and unstable manifolds and the symmetry axes. The stable manifold $W_s$ starting at $P$ transversely intersects $S_1$ at $v$ and $S_2$ at $u$ in this order and the unstable manifold $W_u$ starting at $P$ transversely intersects $S_2$ at $u$ and $S_1$ at $v$ in this order. The two manifolds, $W_s$ and $W_u$, transversely intersect at homoclinic points $u$ and $v$.[20)]

Let us denote by $[\alpha, \beta]_A$ an open arc of one-dimensional manifold $A$ with $\alpha, \beta \in A$. If $A$ has an orientation, we use the convention that the up-stream point is the left terminal of the interval. A closed arc $[\alpha, \beta]_A$ and a semi-open arc $(\alpha, \beta]_A$ are also defined. We next introduce the arcs $\gamma_u = [u, v]_{W_u}$, $\gamma_s = [u, v]_{W_s}$, $\Gamma_u = [v, Tu]_{W_u}$ and $\Gamma_s = [v, Tu]_{W_s}$. The homoclinic lobe $U$ is an open region bounded by $\gamma_u$ and $\gamma_s$, and the homoclinic lobe $V$ is an open region bounded by $\Gamma_u$ and $\Gamma_s$. Finally, we introduce the closed region $Z$ bounded by the four arcs $[P, u]_{W_u}$, $[u, v]_{W_s}$, $[v, Tu]_{W_u}$ and $[Tu, P]_{W_s}$. The geometry is displayed in Fig. 1.

Next we consider the situation for $a = a_{\rm hs}$, the value at which the horseshoe is just completed (see Fig. 2). There exist four components of $\mathrm{int}\{TZ \cap T^{-1}Z\}$, where

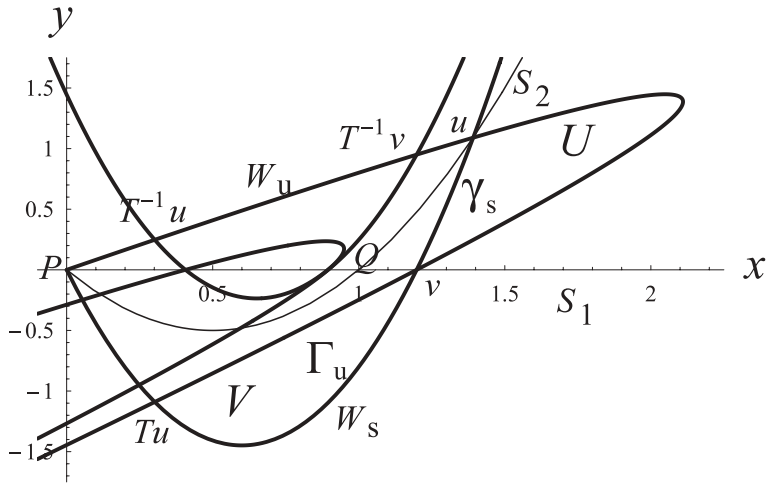


Fig. 1. The stable and unstable manifolds $W_s$ and $W_u$ of a saddle $P$, the homoclinic lobes $U$ and $V$, two homoclinic intersection points $u$ and $v$, and the two symmetry axes $S_1$ (the $x$-axis) and $S_2$ are displayed for $a = 4$.

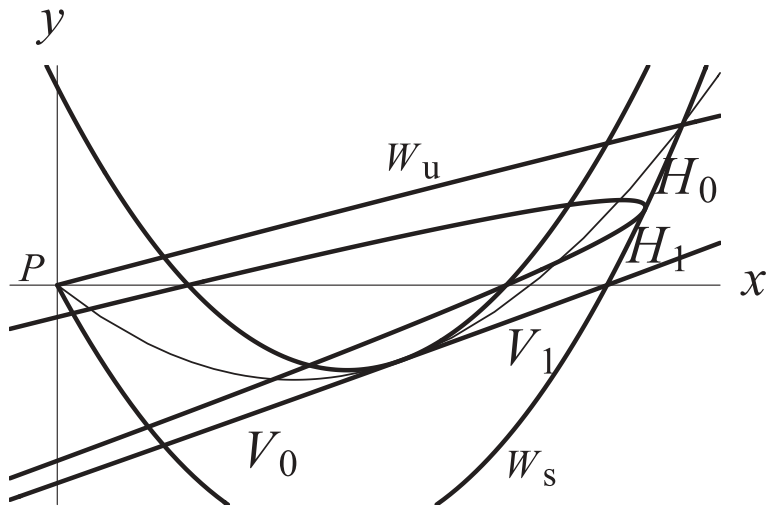


Fig. 2. The structure of $W_s$ and $W_u$ in the situation that the horseshoe is just completed. $V_0$ and $V_1$ are the two vertical belts in $Z \cap T^{-1}Z$, and $H_0$ and $H_1$ are the two horizontal belts in $Z \cap TZ$.

int$\{A\}$ denotes the interior of set $A$. The region defined by $V_0 \cap H_0$ (resp., $V_1 \cap H_1$) includes $P$ (resp., $Q$). It is well known that $h_{\rm top} = \ln 2$ for $a \geq a_{\rm hs}$. If the orbital point is located in $V_0$ (resp., $V_1$), its symbol is defined as 0 (resp., 1). With this rule, we determine the symbol sequence for a periodic orbit. There is no ambiguity in this determination, because the common point of $V_0$ and $V_1$ is a homoclinic point and is not periodic.

The following proposition is important when we consider the origin of the plateau regions. The proof is given in Ref. 5).

**Proposition 1**. Neither $U$ nor $V$ contains any periodic orbits.

2.2. *Intervals in symmetry axes*

In the following, we use four segments of the symmetry axes, defined as follows:

$$S_{11} \equiv \{(x, y) : y = 0,\ 0 < x < 1\}, \tag{10}$$
$$S_{12} \equiv \{(x, y) : y = 0,\ 1 < x < \pi_1(v)\}, \tag{11}$$
$$S_{21} \equiv \{(x, y) : y = -f(x)/2,\ 0 < x < 1\}, \tag{12}$$
$$S_{22} \equiv \{(x, y) : y = -f(x)/2,\ 1 < x < \pi_1(u)\}. \tag{13}$$

Here, $\pi_1(z)$ represents the $x$-coordinate of the point $z$. Similarly, $\pi_2(z)$ is used to represent the $y$-coordinate of $z$.

We next define several kinds of intervals in $S_{11}$ and $S_{21}$:

$$I_i \equiv T^{-i}U \cap S_{11} = (A_i, B_i), \tag{14}$$
$$L_i \equiv (B_{i+1}, A_i), \tag{15}$$
$$J_i \equiv T^{-i}U \cap S_{21} = (C_i, D_i), \tag{16}$$
$$M_i \equiv (D_{i+1}, C_i). \tag{17}$$

Here, we have $\pi_1(A_i) < \pi_1(B_i)$ and $\pi_1(C_i) < \pi_1(D_i)$ for $i \geq 1$.

Let us denote by $O(z_0) = \{\cdots, z_{-1}, z_0, z_1, z_2, \cdots\}$ the orbit of a point $z_0$. If $z_0$ is a periodic point of period $q$, we can write its orbit as $O(z_0) = \{z_0, z_1, \cdots, z_{q-1}\}$. In the case of a symmetric periodic orbit $O(z_0)$ for which $z_0 \in L_i$, $z_k \in M_j$ and the points $z_m$ for $0 < m < k$ are not located on any symmetry axis. Its period is $q = 2k+1$ as seen from the theorem of de Vogelaere.[3] In §3, we derive the dynamical ordering for these periodic orbits.

The following proposition relates the forward and backward images of the arcs of the symmetry axes with the stable and unstable manifolds. This proposition is a direct consequence of the Lambda lemma.[21]

**Proposition 2**.

$$\lim_{i\to\infty} T^{i+1}L_i = \Gamma_u = \lim_{i\to\infty} T^{i+2}M_{i+1}, \tag{18}$$
$$\lim_{i\to\infty} T^{-(i+1)}L_i = \gamma_s = \lim_{i\to\infty} T^{-(i+1)}M_{i+1}. \tag{19}$$

Equation (19) is derived from Eq. (18) by using the relations $hT^{i+1}L_i = T^{-(i+1)}hL_i = T^{-(i+1)}L_i$ and $hT^{i+2}M_{i+1} = gT^{i+1}M_{i+1} = T^{-(i+1)}gM_{i+1} = T^{-(i+1)}M_{i+1}$. The arcs of the images of $L_i$ and $M_{i+1}$ in Eq. (18) are located on the right side of $\Gamma_u$ with respect to the orientation of $\Gamma_u$, and those of the inverse images of $L_i$ and $M_{i+1}$ in Eq. (19) are located on the right side of $\gamma_s$.

2.3. *Procedures of the trellis method and the DOM*

Here we summarize the trellis method and the DOM.

**Algorithm of the trellis method**[8]

[1] Define the trellis by the segments of the stable and unstable manifolds.

[2] Draw one control edge (c-edge) for each stable segment in the trellis.

[3] Join two adjacent c-edges with one expanding edge (e-edge). The set of c-edges and e-edges is called a compatible graph $\mathcal{G}$.
[4] Determine the images of the c-edges.
[5] If there is an invariant set of edges of $\mathcal{G}$ which does not contain a c-edge, then collapse each of these edges to a point.
[6] After deleting the e-edges not contributing to the transition matrix $M$, we obtain a simplified graph $\widehat{\mathcal{G}}$.
[7] Construct the transition matrix $M$ and calculate its eigenvalues. The lower bound of the topological entropy thus obtained is $\ln \lambda_{\max}$, where $\lambda_{\max}$ is the largest eigenvalue of $M$.

**Procedure of the dynamical ordering method (DOM)**
[1] Consider tangent stable and unstable manifolds.
[2] Construct the dynamical ordering (DO) for the symmetric periodic orbits appearing through saddle-node bifurcations before and after tangency.
[3] Define the symbol sequences for the symmetric periodic orbits included in the list of the DO.
[4] Use the symbol sequence and the software *Wintrain*, developed by Hall, to calculate the largest eigenvalue $\hat{\lambda}_{\max}$, for which we have $h_{\text{top}} \geq \ln \hat{\lambda}_{\max}$.

## §3. Dynamical ordering

### 3.1. *A theorem*

In this subsection, we prove Theorem 1, which asserts the existence of the dynamical orderings for the symmetric periodic orbits appearing through saddle-node bifurcations.

*Theorem 1.* Let $k \geq 0$ and $k' \geq 0$ be integers that are not simultaneously zero. Suppose that $T^k \Gamma_u$ and $T^{-k'} \gamma_s$ have a quadratic tangency point at $a = a_c(k'')$, with $k'' = k + k'$, and have transversal intersection points for $a > a_c(k'')$. Let $i_c(k'')$ (abbreviated as $i_c$) be the suffix $i$ of $L_i$ which appears at $a = a_c(k'')$ due to the tangency of $T^k \Gamma_u$ and $T^{-k'} \gamma_s$. Then, the dynamical orderings of Types I, II, III and IV hold.
*Remarks.* Here we explain how to read Tables I(a), (b), (c) and (d) 1) The quantities indicated by $L_i$ in the left box and $M_i$ in the top box are the intervals in the symmetry axes defined in §2.2. The symbol '$\Rightarrow$' represents a forcing relation between intervals. Thus, for example, $M_{i_c+1} \Rightarrow M_{i_c+2}$ means that if $M_{i_c+1}$ exists, then $M_{i_c+2}$ exists. The symbol '$\Downarrow$' represents the same relation. 2) The numbers in the main box are the periods of the periodic orbits that appear through saddle-node bifurcations. If a number is in the column labeled by, say, $M_{i_c+1}$, then the periodic orbit with this period has an orbital point in $M_{i_c+1}$. Similarly, if a number is in the row labeled by, say, $L_{i_c}$, then the periodic orbit with this period has an orbital point in $L_{i_c}$. These periodic orbits are symmetric, because they have two orbital points on symmetry axes. 3) All the numbers in the main box belong to a row and a column. If a number is in column $M_{i_c+l}$ and row $L_{i_c+m}$, then the period of the corresponding

Table I. (a) Dynamical ordering of Type I.

| | $M_{i_c+1}$ | $\Rightarrow$ | $M_{i_c+2}$ | $\Rightarrow$ | $M_{i_c+3}$ | $\Rightarrow$ |
|---|---|---|---|---|---|---|
| $L_{i_c}$ | $2(k+k')+4i_c+5$ | $\leftarrow$ | $2(k+k')+4i_c+7$ | $\leftarrow$ | $2(k+k')+4i_c+9$ | $\leftarrow$ |
| $\Downarrow$ | $\uparrow$ | | $\uparrow$ | | $\uparrow$ | |
| $L_{i_c+1}$ | $2(k+k')+4i_c+7$ | $\leftarrow$ | $2(k+k')+4i_c+9$ | $\leftarrow$ | $2(k+k')+4i_c+11$ | $\leftarrow$ |
| $\Downarrow$ | $\uparrow$ | | $\uparrow$ | | $\uparrow$ | |
| $L_{i_c+2}$ | $2(k+k')+4i_c+9$ | $\leftarrow$ | $2(k+k')+4i_c+11$ | $\leftarrow$ | $2(k+k')+4i_c+13$ | $\leftarrow$ |
| $\Downarrow$ | $\uparrow$ | | $\uparrow$ | | $\uparrow$ | |
| $L_{i_c+3}$ | $2(k+k')+4i_c+11$ | $\leftarrow$ | $2(k+k')+4i_c+13$ | $\leftarrow$ | $2(k+k')+4i_c+15$ | $\leftarrow$ |
| $\Downarrow$ | $\uparrow$ | | $\uparrow$ | | $\uparrow$ | |

(b) Dynamical ordering of Type II.

| | $M_{i_c+1}$ | $\Rightarrow$ | $M_{i_c+2}$ | $\Rightarrow$ | $M_{i_c+3}$ | $\Rightarrow$ |
|---|---|---|---|---|---|---|
| $L_{i_c}$ | $2(k+k')+4i_c+5$ | $\leftarrow$ | $2(k+k')+4i_c+7$ | $\leftarrow$ | $2(k+k')+4i_c+9$ | $\leftarrow$ |
| $\Downarrow$ | $\downarrow$ | | $\downarrow$ | | $\downarrow$ | |
| $L_{i_c+1}$ | $2(k+k')+4i_c+7$ | $\leftarrow$ | $2(k+k')+4i_c+9$ | $\leftarrow$ | $2(k+k')+4i_c+11$ | $\leftarrow$ |
| $\Downarrow$ | $\downarrow$ | | $\downarrow$ | | $\downarrow$ | |
| $L_{i_c+2}$ | $2(k+k')+4i_c+9$ | $\leftarrow$ | $2(k+k')+4i_c+11$ | $\leftarrow$ | $2(k+k')+4i_c+13$ | $\leftarrow$ |
| $\Downarrow$ | $\downarrow$ | | $\downarrow$ | | $\downarrow$ | |
| $L_{i_c+3}$ | $2(k+k')+4i_c+11$ | $\leftarrow$ | $2(k+k')+4i_c+13$ | $\leftarrow$ | $2(k+k')+4i_c+15$ | $\leftarrow$ |
| $\Downarrow$ | $\downarrow$ | | $\downarrow$ | | $\downarrow$ | |

(c) Dynamical ordering of Type III.

| | $M_{i_c+1}$ | $\Rightarrow$ | $M_{i_c+2}$ | $\Rightarrow$ | $M_{i_c+3}$ | $\Rightarrow$ |
|---|---|---|---|---|---|---|
| $L_{i_c}$ | $2(k+k')+4i_c+5$ | $\rightarrow$ | $2(k+k')+4i_c+7$ | $\rightarrow$ | $2(k+k')+4i_c+9$ | $\rightarrow$ |
| $\Downarrow$ | $\uparrow$ | | $\uparrow$ | | $\uparrow$ | |
| $L_{i_c+1}$ | $2(k+k')+4i_c+7$ | $\rightarrow$ | $2(k+k')+4i_c+9$ | $\rightarrow$ | $2(k+k')+4i_c+11$ | $\rightarrow$ |
| $\Downarrow$ | $\uparrow$ | | $\uparrow$ | | $\uparrow$ | |
| $L_{i_c+2}$ | $2(k+k')+4i_c+9$ | $\rightarrow$ | $2(k+k')+4i_c+11$ | $\rightarrow$ | $2(k+k')+4i_c+13$ | $\rightarrow$ |
| $\Downarrow$ | $\uparrow$ | | $\uparrow$ | | $\uparrow$ | |
| $L_{i_c+3}$ | $2(k+k')+4i_c+11$ | $\rightarrow$ | $2(k+k')+4i_c+13$ | $\rightarrow$ | $2(k+k')+4i_c+15$ | $\rightarrow$ |
| $\Downarrow$ | $\uparrow$ | | $\uparrow$ | | $\uparrow$ | |

(d) Dynamical ordering of Type IV.

| | $M_{i_c+1}$ | $\Rightarrow$ | $M_{i_c+2}$ | $\Rightarrow$ | $M_{i_c+3}$ | $\Rightarrow$ |
|---|---|---|---|---|---|---|
| $L_{i_c}$ | $2(k+k')+4i_c+5$ | $\rightarrow$ | $2(k+k')+4i_c+7$ | $\rightarrow$ | $2(k+k')+4i_c+9$ | $\rightarrow$ |
| $\Downarrow$ | $\downarrow$ | | $\downarrow$ | | $\downarrow$ | |
| $L_{i_c+1}$ | $2(k+k')+4i_c+7$ | $\rightarrow$ | $2(k+k')+4i_c+9$ | $\rightarrow$ | $2(k+k')+4i_c+11$ | $\rightarrow$ |
| $\Downarrow$ | $\downarrow$ | | $\downarrow$ | | $\downarrow$ | |
| $L_{i_c+2}$ | $2(k+k')+4i_c+9$ | $\rightarrow$ | $2(k+k')+4i_c+11$ | $\rightarrow$ | $2(k+k')+4i_c+13$ | $\rightarrow$ |
| $\Downarrow$ | $\downarrow$ | | $\downarrow$ | | $\downarrow$ | |
| $L_{i_c+3}$ | $2(k+k')+4i_c+11$ | $\rightarrow$ | $2(k+k')+4i_c+13$ | $\rightarrow$ | $2(k+k')+4i_c+15$ | $\rightarrow$ |
| $\Downarrow$ | $\downarrow$ | | $\downarrow$ | | $\downarrow$ | |

orbits is $2(k+k')+4i_c+2(l+m)+3$, the initial point $z_0$ is in $L_{i_c+m}$, and the point $z_{k+k'+2i_c+l+m+1}$ is in $M_{i_c+l}$. 4) The symbol '$\leftarrow$' represents a forcing relation between periodic orbits. Let us consider one relation from these tables:

$$q' \leftarrow q. \tag{20}$$

We read Eq. (20) as "$q$ forces $q'$". This means that the existence of a point of a

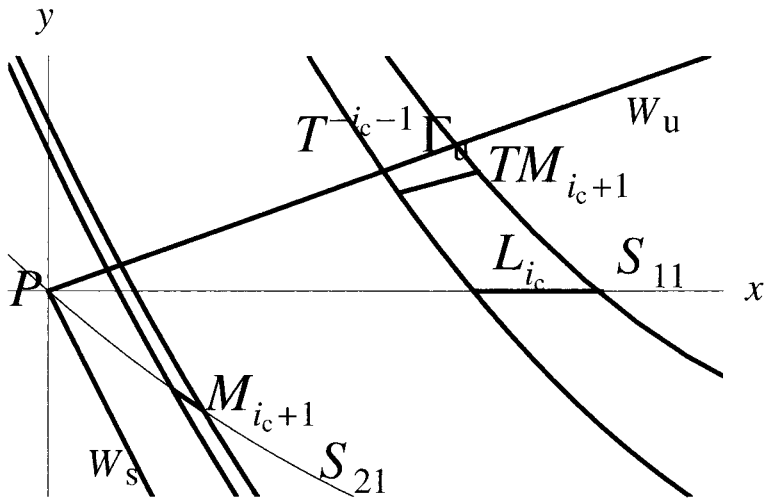


Fig. 3. Relations among $T^{-i_c-1}\Gamma_u$, $TM_{i_c+1}$ and $L_{i_c}$.

periodic orbit with period $q$ implies the existence of a point of a periodic orbit with period $q'$. We also use the symbols $\rightarrow$, $\uparrow$ and $\downarrow$ to express the same forcing relation.

*Proof.* Two arcs $\gamma_s$ and $\Gamma_u$ have no common points except $v$. Thus, the case $k = k' = 0$ is excluded in Theorem 1.

If the interval $L_{i_c+m}$ exists, then the interval $M_{i_c+m+1}$ exists for any $m \geq 0$. In fact, $T^{-1}A_{i_c+m}$ $(= g \circ hA_{i_c+m} = gA_{i_c+m})$ is located below $S_{21}$, because $A_{i_c+m}$ is located above $S_{21}$. This fact implies the assertion. In addition, obviously $L_m \Rightarrow L_{m+1}$ and $M_m \Rightarrow M_{m+1}$ for any $m \geq 1$. Thus, the forcing relations between intervals expressed by '$\Rightarrow$' and '$\Downarrow$' in Tables I(a), (b), (c) and (d) have been demonstrated. The interval $TM_{i_c+m+1}$ is situated between $L_{i_c+m}$ and $T^{-i_c-m-1}\Gamma_u$. This relation is displayed for $m = 0$ in Fig. 3.

Suppose that $T^k\Gamma_u$ and $T^{-k}\gamma_s$ $(= hT^k\Gamma_u)$ intersect each other (see Fig. 4). In this situation, the arc $T^{k+i_c+2}M_{i_c+1}$ is located between $T^{k+i_c+1}L_{i_c}$ and $T^k\Gamma_u$. Then, by reversibility, $T^{-k-i_c-1}M_{i_c+1}$ is located between $T^{-k-i_c-1}L_i$ and $T^{-k}\gamma_s$. Here, the relations $hT^{k+i_c+2}M_{i_c+1} = gT^{k+i_c+1}$ $M_{i_c+1} = T^{-k-i_c-1}gM_{i_c+1} = T^{-k-i_c-1}M_{i_c+1}$, $hT^{k+i_c+1}L_{i_c} = T^{-k-i_c-1}hL_{i_c} = T^{-k-i_c-1}L_{i_c}$ and $hT^k\Gamma_u = T^{-k}h\Gamma_u = T^{-k}\gamma_s$ have been used. Operating with $T^{-k'+k}$ on the latter three arcs, we obtain $T^{-k'-i_c-1}M_{i_c+1}$, $T^{-k'}\gamma_s$ and $T^{-k'+i_c+1}L_{i_c}$. The relative positions of these arcs with respect to $T^k\Gamma_u$ and its accompanying arcs in a typical situation are illustrated in Figs. 5(a), (b), (c) and (d). The arc $T^{k+i_c+j+2}L_{i_c+j+1}$ is located between $T^{k+i_c+j+1}L_{i_c+j}$ and $T^k\Gamma_u$ for $j \geq 0$, whereas the arc $T^{-k'-i_c-m-1}M_{i_c+m+1}$ is located between $T^{-k'-i_c-m}M_{i_c+m}$ and $T^{-k'}\gamma_s$ for $m \geq 1$. For $i \geq i_c$, Proposition 2 gives the following relations:

$$\lim_{i\to\infty} T^{k+i+1}L_i = T^k\Gamma_u, \tag{21}$$

$$\lim_{i\to\infty} T^{-(k'+i+1)}M_{i+1} = T^{-k'}\gamma_s. \tag{22}$$

There are four types of tangency. The first type, illustrated in Fig. 5(a), is

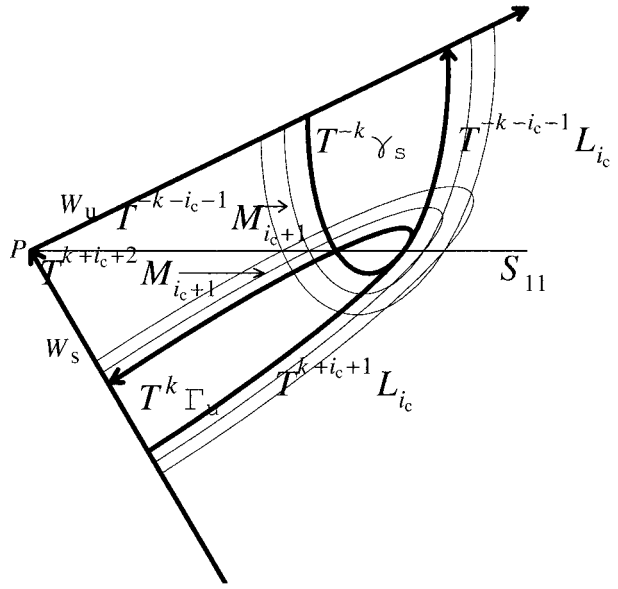


Fig. 4. Schematic illustration of the relations between $T^k\Gamma_u$ and $T^{-k}\gamma_s$, between $T^{k+i_c+1}L_{i_c}$ and $T^{-k-i_c-1}L_{i_c}$, and between $T^{k+i_c+2}M_{i_c+1}$ and $T^{-k-i_c-1}M_{i_c+1}$.

called Type I. The second type, illustrated in Fig. 5(b), is called Type II. The third and fourth types are illustrated in Figs. 5(c) and (d) and called Types III and IV. In Figs. 5(a) and (b), the arc $T^{-k'}\gamma_s$ moves up and exhibits a quadratic tangency with $T^k\Gamma_u$ when the parameter value changes monotonically. In Figs. 5(c) and (d), $T^k\Gamma_u$ moves up and is quadratically tangent to $T^{-k'}\gamma_s$. (However, note that the order, i.e., quadratic or higher, of the tangency is not important in our proof. We only need the following progression as the parameter value changes: non-tangency, tangency and intersection.)

Now, let us consider the case of Type I. Before the tangency of $T^{-k'}\gamma_s$ and $T^k\Gamma_u$, all the periodic orbits included in Table I(a) appear through a saddle-node bifurcation, since all the accompanying arcs exhibit tangencies beforehand. In fact, let us imagine sitting at $T^{k+i_c+1}L_{i_c}$ and watching how the image arcs of $M_{i_c+m}$ $(m \geq 1)$ approach. Before the tangency of $T^{-k'}\gamma_s$ and $T^k\Gamma_u$, $T^{-k'-i_c-1}M_{i_c+1}$ and $T^{k+i_c+1}L_{i_c}$ are tangent. Next, $T^{-k'-i_c-2}M_{i_c+2}$ and $T^{k+i_c+1}L_{i_c}$ become tangent and so on. Thus, the dynamical order relations

$$L_{i_c} : 2(k+k') + 4i_c + 5 \leftarrow 2(k+k') + 4i_c + 7 \leftarrow 2(k+k') + 4i_c + 9 \leftarrow \cdots \qquad (23)$$

are obtained. A periodic orbit of period $2(k+k')+4i_c+5$ has a point in $M_{i_c+1}$. There is a similar situation for the other periodic orbits. Similarly, sitting at $T^{k+i_c+1}L_{i_c+l}$, $l \geq 1$ and watching the image arcs of $M_{i_c+m}$ $(m \geq 1)$, we obtain the dynamical ordering indicated by the symbol $\leftarrow$.

Next, let us imagine sitting at $T^{-k'-i_c-1}M_{i_c+1}$ and looking around. This arc has a tangency point with $T^{k+i_c+1}L_{i_c}$, $T^{k+i_c+2}L_{i_c+1}$, $\cdots$, in this order, as the value of the parameter $a$ increases. This implies the dynamical ordering in the first column. Similarly, sitting at $T^{-k'-i_c-m}M_{i_c+m}$ $(m \geq 2)$ and looking around, we obtain the

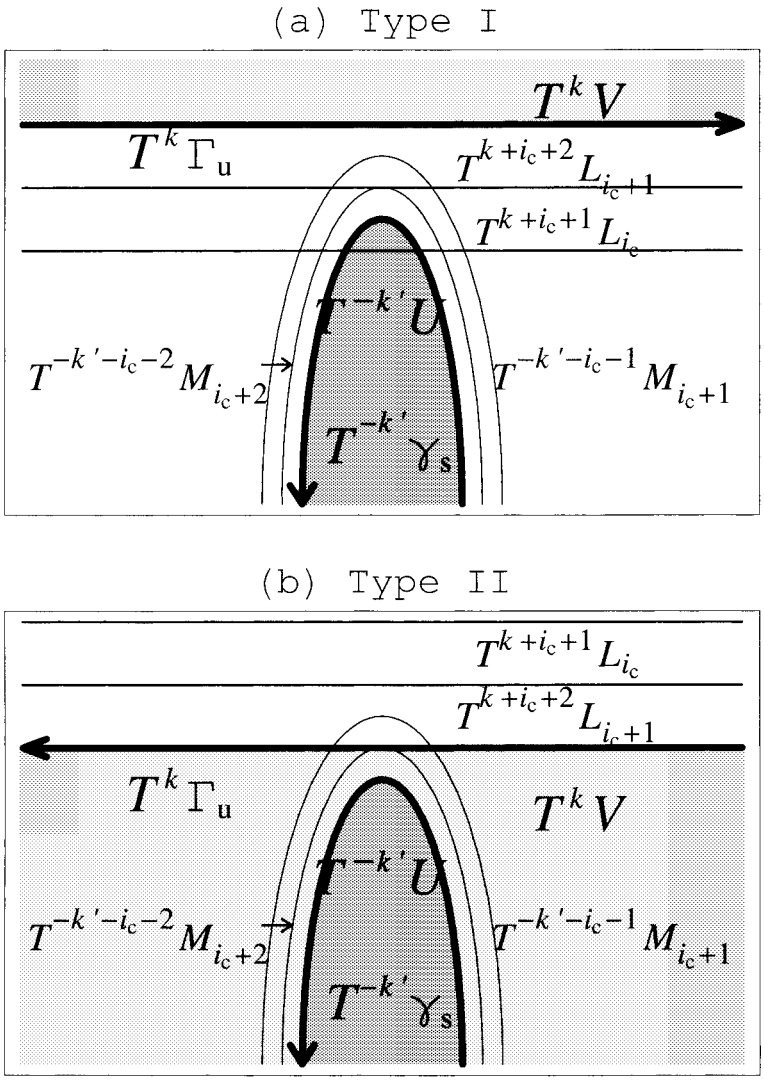


Fig. 5. Schematic illustrations of the four tangency situations for $T^k \Gamma_u$ and $T^{-k'} \gamma_s$. In (a) and (b), the top of $T^{-k'} \gamma_s$ moves up and has a quadratic tangency point with $T^k \Gamma_u$. In (a), the gray region above $T^k \Gamma_u$ is included in $T^k V$, and the dark gray region below $T^{-k'} \gamma_s$ is included in $T^{-k'} U$. The situation is similar in (b).

dynamical ordering indicated by $\uparrow$. Thus the proof for Type I is completed.

Next, using Fig. 5(b), let us verify the dynamical ordering of Type II. We assume that the top of arc $T^{-k'} \gamma_s$ moves up and has a tangency point on $T^k \Gamma_u$. Before the appearance of this tangency, there is the situation in which $T^{-k'-i_c-1} M_{i_c+1}$ is tangent to $T^k \Gamma_u$. After this tangency, $T^{-k'-i_c-1} M_{i_c+1}$ intersects the images of $L_{i_c}$. This process gives the following ordering:

$$M_{i_c+1} : 2(k+k') + 4i_c + 5 \to 2(k+k') + 4i_c + 7 \to 2(k+k') + 4i_c + 9 \to \cdots . \quad (24)$$

This is the dynamical ordering of the first column in Table I(b). The proofs for the

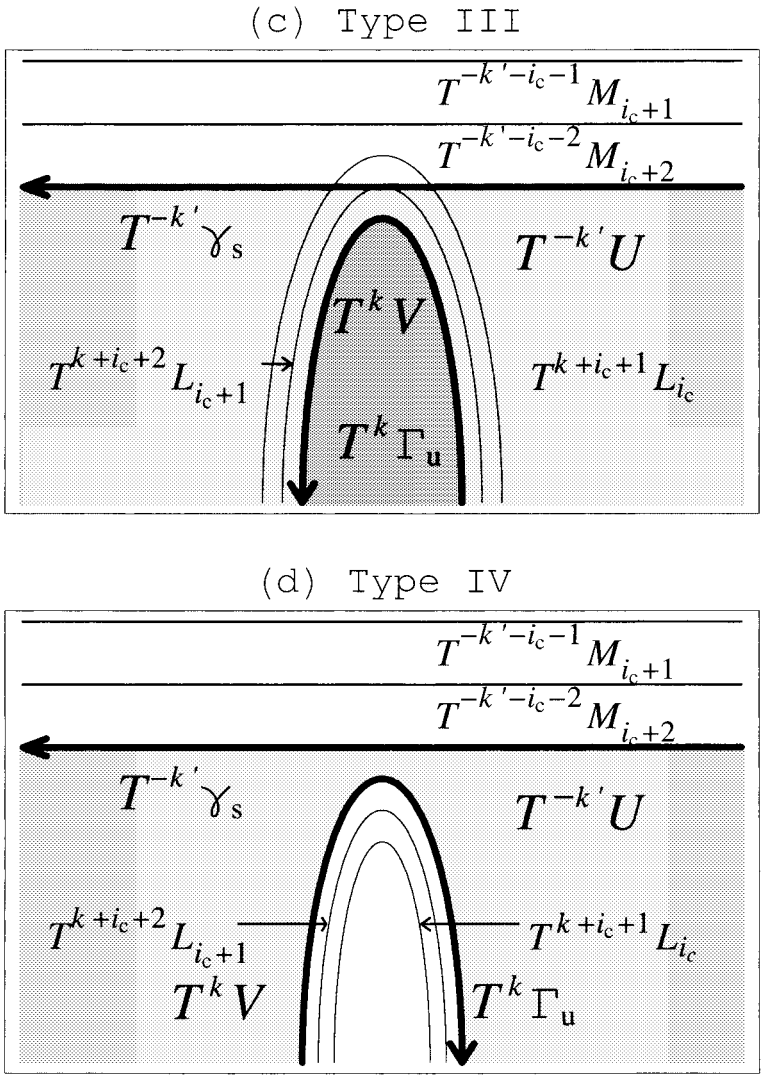


Fig. 5 (continued). In (c) and (d), the top of $T^k\Gamma_u$ moves up and has a quadratic tangency point with $T^{-k'}\gamma_s$. In (c), the gray region below $T^{-k'}\gamma_s$ is included in $T^{-k'}U$, and the dark gray region below $T^k\Gamma_u$ is included in $T^kV$. In (d), the gray region is included in both $T^kV$ and $T^{-k'}U$.

other columns are similar and thus omitted.

Let us now imagine observing the process while sitting at $T^{k+i_c+1}L_{i_c}$. First, $T^{-k'-i_c-1}M_{i_c+1}$ approaches and becomes tangent to $T^{k+i_c+1}L_{i_c}$. Next, $T^{-k'-i_c-2}M_{i_c+2}$ becomes tangent to $T^{k+i_c+1}L_{i_c}$. Thus, the dynamical ordering of the first row is proved. The proof for the other rows is similar and therefore omitted.

The situations for Types III and IV are displayed in Figs. 5(c) and (d). Here we note how these situations are realized. The higher iterates of $\Gamma_u$ are also folded when they accumulate at $T^k\Gamma_u$. Then there is an iterate $T^m\Gamma_u$ $(m > k)$ that remains below and runs parallel to $T^k\Gamma_u$ but whose orientation is reversed [see Fig. 5(a) for

reference]. In this case, higher iterates of $L_{i_c+j}$ ($j \gg 1$) remain above and run parallel to $T^m \Gamma_u$. This is the situation illustrated in Fig. 5(c). The situation illustrated in Fig. 5(d) can be realized similarly. Using these figures, we can prove the dynamical orderings of Types III and IV. However, we omit the details of the proof. (Q.E.D.)

### 3.2. *Remarks on Theorem 1*

In order to specify the periodic orbit in Tables I(a)–(d), we use the matrix notation $(i, j)$, where $i$ is the suffix of the interval $L_i$ and $j$ is that of $M_j$. Let $a_c^{\mathrm{I(a)}}(i, j)$ be the critical parameter value at which the periodic orbit of the $(i, j)$-element in Table I(a) appears through a saddle-node bifurcation. The critical values $a_c^{\mathrm{I(b)}}(i, j)$, $a_c^{\mathrm{I(c)}}(i, j)$ and $a_c^{\mathrm{I(d)}}(i, j)$ are defined similarly. The following relations hold:

$$\lim_{i,j\to\infty} a_c^{\mathrm{I(a)}}(i, j) = a_c^{\mathrm{I(a)}}(k''), \tag{25}$$

$$\lim_{i,j\to\infty} a_c^{\mathrm{I(b)}}(i, j) = a_c^{\mathrm{I(b)}}(k''), \tag{26}$$

$$\lim_{i,j\to\infty} a_c^{\mathrm{I(c)}}(i, j) = a_c^{\mathrm{I(c)}}(k''), \tag{27}$$

$$\lim_{i,j\to\infty} a_c^{\mathrm{I(d)}}(i, j) = a_c^{\mathrm{I(d)}}(k''). \tag{28}$$

All the periodic orbits included in Table I(a) appear before the tangency of $T^k \Gamma_u$ and $T^{-k'} \gamma_s$. Contranstingly, all the periodic orbits in Table I(d) appear after the tangency. Some periodic orbits in Tables I(b) and (c) appear before the tangency and others appear after.

Let us now briefly consider the order of appearance of the different types of tangency. The region $T^k V$ leaves $Z$ under the backward iteration. Therefore we regard $T^k V$ as a region located outside of $Z$. The top of $T^{-k'} \gamma_s$ leaves $Z$ through a condition of tangency and returns to $Z$ through a second condition of tangency. This implies that the tangency of Type II appears after the tangency of Type I. Here we consider the situation in which the value of $a$ increases. Let us consider the case with $k = 0$, $k' = 1$ and $i_c = 1$. This situation corresponds to the completion of the horseshoe. Before the completion of the horseshoe, the dynamical ordering of Type I appears, but that of Type II does not appear. This is derived from the fact that a portion of $T^{-1} \gamma_s$ leaves $Z$ and never returns. For this case, only the ordering of Type I holds (see §4.7).

For $k$, $k' \gg 1$, the orderings of Types III and IV appear. For example, the tangency of Type III appears after the tangency of Type I, and the tangency of Type IV appears after the tangency of Type II. It is difficult to realize these tangency situations through numerical calculation. In the following section, we study the tangencies of Types I and II.

## §4. Just before the completion of horseshoe

### 4.1. *Definition of the n-th stage*

We now consider the situation before the completion of the horseshoe and suppose that $T^{-1}\gamma_s$ does not yet intersect $S_{21}$. However, $T^{-1}\gamma_s$ may intersect $S_{11}$. In this case, $T^{-2}\gamma_s$ intersects $S_{21}$. We consider the situation in which $T^{-2}\gamma_s$ intersects $S_{21}$, $S_{12}$ and $S_{22}$ and has a tangency point in $T^2\Gamma_u$ (see Fig. 6). We easily confirm that this takes place for $a = a_l^{(1)} < a_{\rm hs}$. Increasing the value of $a$ further, the top of arc $T^{-2}\gamma_s$ moves up, and then it again has a tangency point in $T^2\Gamma_u$. Let $a = a_r^{(1)} < a_{\rm hs}$ be the parameter value in this situation. Let us call the parameter range $[a_l^{(1)}, a_r^{(1)}]$ the "first stage". The geometrical configurations of the stable and unstable manifolds for the beginning and end of the first stage are displayed in Fig. 6.

The situation before the first stage is schematically illustrated in Fig. 7. With the increase of the value of $a$, the top of arc $T^{-2}\gamma_s$ moves up and intersects first the lower side of the folded $T^2\Gamma_u$ and then the upper side. These two intersections, or more precisely, tangencies define the first stage. If the value of $a$ is increased further, the top of arc $T^{-2}\gamma_s$ moves up and then intersects first the lower side of the folded $T^3\Gamma_u$, which corresponds to the start of the second stage, and then the upper side, which corresponds to the end of the second stage. We write this parameter range as $[a_l^{(2)}, a_r^{(2)}]$. The beginning and end of the $n$-th stage are defined similarly. Thus, the situation in which $T^{-2}\gamma_s$ is tangent to $T^{n+1}\Gamma_u$ whose direction is to the right (resp., left) is the beginning (resp., end) of the $n$-th stage. This stage is denoted $[a_l^{(n)}, a_r^{(n)}]$.

### 4.2. *The first stage*

From the structure of $W_u$ and $W_s$ displayed in the upper panel of Fig. 6, we define the trellis displayed in Fig. 8 (the upper panel) and construct its compatible graph (the lower panel). Next, we follow the images of the control edges labeled $A,\ B,\ \cdots, G$. Here the relations $\beta = T\alpha$ and $\gamma = T\beta$ hold. In this way, all elements of the transition matrix $M_1$ are obtained.[8)]

$$M_1 = \left(\begin{array}{c|ccccccc} & B & C & E & F & D & A & G \\ \hline B & 0 & 0 & 0 & 0 & 0 & 1 & 0 \\ C & 0 & 1 & 0 & 1 & 2 & 0 & 2 \\ E & 1 & 0 & 0 & 0 & 0 & 0 & 0 \\ F & 0 & 1 & 1 & 0 & 0 & 0 & 0 \\ D & 0 & 0 & 1 & 0 & 0 & 0 & 0 \\ A & 0 & 0 & 1 & 1 & 0 & 1 & 0 \\ G & 0 & 0 & 0 & 0 & 1 & 0 & 0 \end{array}\right). \tag{29}$$

The element corresponding to the transitions from $C$ to $D$ and from $C$ to $G$ is 2. This is due to the fact that the image of $C$ covers $D$ and $G$ twice. The characteristic equation

$$\lambda^7 - 2\lambda^6 + 2\lambda^2 - 2\sum_{k=0}^{1}\lambda^k = 0 \tag{30}$$

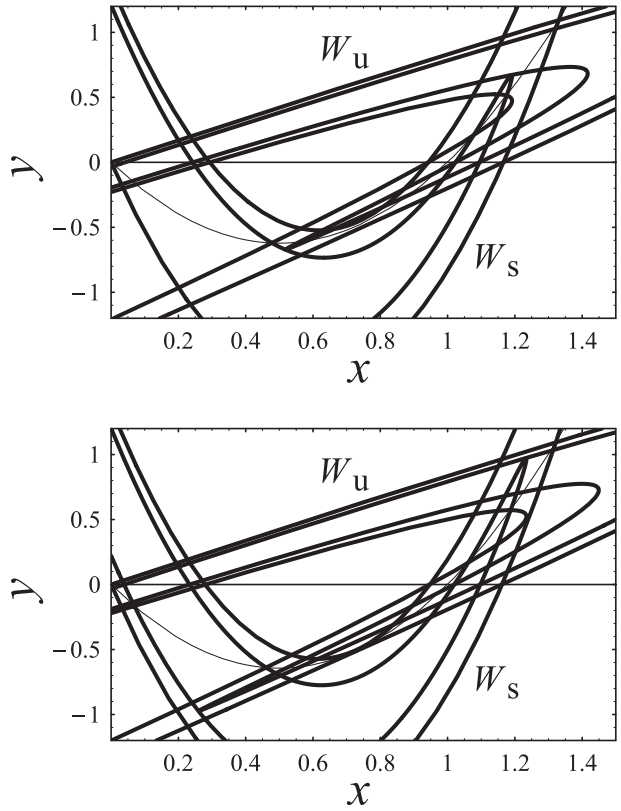


Fig. 6. The upper figure depicts the beginning ($a = 4.975$) of the first stage and the lower figure the end ($a = 5.145$) of the first stage.

gives the largest eigenvalue, $\lambda_{\max} = 1.9688$. This value is equal to that of the transition matrix constructed by Davis, Mackay and Sannami (DMS).[17] The dynamical orderings in these situations are included in Theorem 1 with $k = k' = 2$ and $i_c = 1$. These are obtained in Tables II(a) and II(b).

The completion of the horseshoe is equivalent to the existence of tangency between $T^{-2}\gamma_s$ and $T^{-1}\Gamma_u$. In this situation, $T^{-2}\gamma_s$ and $T^2\Gamma_u$ already intersect each other, and hence Theorem 1 applies with $k = k' = 2$, and $i_c = 1$. This gives us the periodic orbits appearing in Tables II(a) and II(b) that correspond to Tables I(a) and I(b). The two periodic orbits appearing through the saddle-node bifurcation have the following symbol sequences:

$$s^1_{\mathrm{II.(a)}}(i,j) = \begin{cases} 0^i(110111)0^{2j-1}(111011)0^i, \\ 0^i(110101)0^{2j-1}(101011)0^i, \end{cases} \tag{31}$$

$$s^1_{\mathrm{II(b)}}(i,j) = \begin{cases} 0^i(100111)0^{2j-1}(111001)0^i, \\ 0^i(100101)0^{2j-1}(101001)0^i. \end{cases} \tag{32}$$

From the symmetry and the numerical calculation, we can determine the symbol sequence for the periodic orbit $O(z_0)$ of period 17 with $z_0 \in L_1$, which is the $(1,2)$-

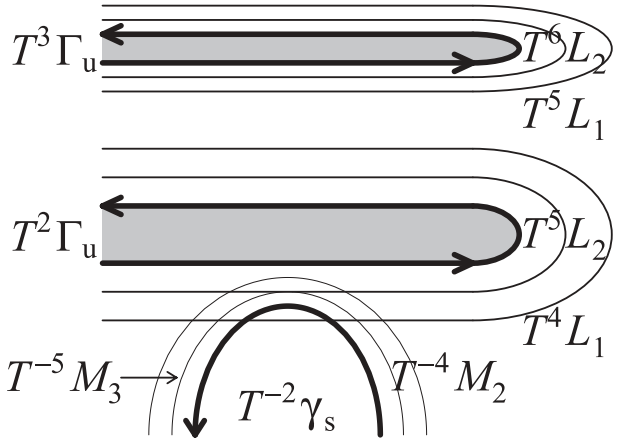


Fig. 7. Schematic illustration of the situation before the first stage. The lower gray region is included in $T^2V$ and the upper one in $T^3V$.

Table II. Dynamical ordering.

(a)

| | $M_2$ | $\Rightarrow$ | $M_3$ | $\Rightarrow$ | $M_4$ | $\Rightarrow$ | $M_5$ | $\Rightarrow\cdots$ |
|---|---|---|---|---|---|---|---|---|
| $L_1$ | 17 | $\leftarrow$ | 19 | $\leftarrow$ | 21 | $\leftarrow$ | 23 | $\leftarrow\cdots$ |
| $\Downarrow$ | $\uparrow$ | | $\uparrow$ | | $\uparrow$ | | $\uparrow$ | |
| $L_2$ | 19 | $\leftarrow$ | 21 | $\leftarrow$ | 23 | $\leftarrow$ | 25 | $\leftarrow\cdots$ |
| $\Downarrow$ | $\uparrow$ | | $\uparrow$ | | $\uparrow$ | | $\uparrow$ | |
| $L_3$ | 21 | $\leftarrow$ | 23 | $\leftarrow$ | 25 | $\leftarrow$ | 27 | $\leftarrow\cdots$ |
| $\Downarrow$ | $\uparrow$ | | $\uparrow$ | | $\uparrow$ | | $\uparrow$ | |
| $L_4$ | 23 | $\leftarrow$ | 25 | $\leftarrow$ | 27 | $\leftarrow$ | 29 | $\leftarrow\cdots$ |
| $\Downarrow$ | $\uparrow$ | | $\uparrow$ | | $\uparrow$ | | $\uparrow$ | |
| $\cdots$ | $\cdots$ | | $\cdots$ | | $\cdots$ | | $\cdots$ | |

(b)

| | $M_2$ | $\Rightarrow$ | $M_3$ | $\Rightarrow$ | $M_4$ | $\Rightarrow$ | $M_5$ | $\Rightarrow\cdots$ |
|---|---|---|---|---|---|---|---|---|
| $L_1$ | 17 | $\leftarrow$ | 19 | $\leftarrow$ | 21 | $\leftarrow$ | 23 | $\leftarrow\cdots$ |
| $\Downarrow$ | $\downarrow$ | | $\downarrow$ | | $\downarrow$ | | $\downarrow$ | |
| $L_2$ | 19 | $\leftarrow$ | 21 | $\leftarrow$ | 23 | $\leftarrow$ | 25 | $\leftarrow\cdots$ |
| $\Downarrow$ | $\downarrow$ | | $\downarrow$ | | $\downarrow$ | | $\downarrow$ | |
| $L_3$ | 21 | $\leftarrow$ | 23 | $\leftarrow$ | 25 | $\leftarrow$ | 27 | $\leftarrow\cdots$ |
| $\Downarrow$ | $\downarrow$ | | $\downarrow$ | | $\downarrow$ | | $\downarrow$ | |
| $L_4$ | 23 | $\leftarrow$ | 25 | $\leftarrow$ | 27 | $\leftarrow$ | 29 | $\leftarrow\cdots$ |
| $\Downarrow$ | $\downarrow$ | | $\downarrow$ | | $\downarrow$ | | $\downarrow$ | |
| $\cdots$ | $\cdots$ | | $\cdots$ | | $\cdots$ | | $\cdots$ | |

element in Table II(a). The symbol for $z_0$ is 0, because $z_0$ is located in $L_1$, $z_8$ is located in $M_2$, and both the intervals $L_1$ and $M_2$ are located in the region $V_0$ of Fig. 2. The two points $z_1$ and $z_4$ are located in the region labeled $V_1 \cap H_0$ in Fig. 2. As $\pi_2(z_4) < \pi_2(x_1)$, the point $z_3$ is located in the region labeled $V_0 \cap H_1$. Hence, the symbol for $z_1$ is 1 and that for $z_3$ is 0. Comparing the positions of $TM_2$ and $L_1$, we see that the symbol for $z_9$ is 0, and consequently the symbol for $z_7$ is 0. We need a numerical calculation to determine the position of $z_2$. The symbol is 1 for $z_2$, as

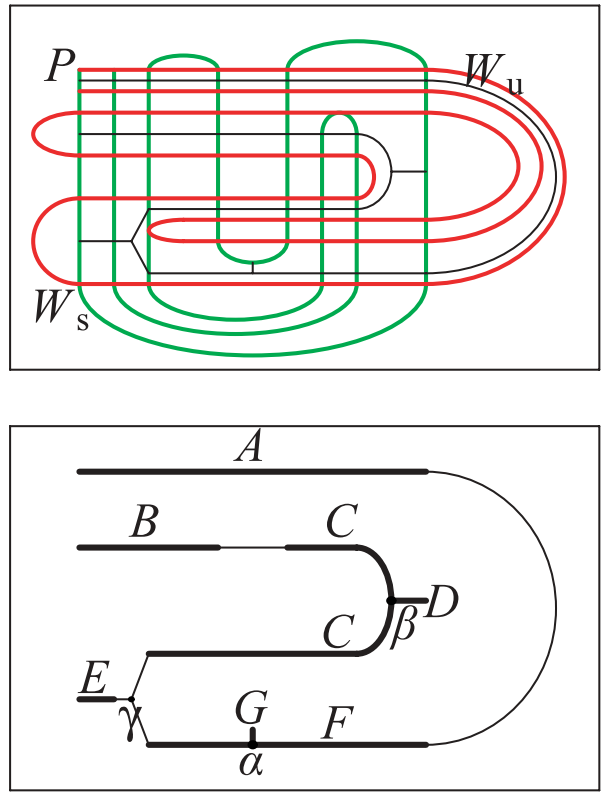


Fig. 8. Trellis (upper graph) in the first stage and its compatible graph $\widehat{\mathcal{G}}$ represented by the thin curve. In the lower figure, the control edges in $\widehat{\mathcal{G}}$ are named $A, B, \cdots, G$. Here, the relations $\beta = T\alpha$ and $\gamma = T\beta$ hold.

shown in Fig. 9. The symbols 1 and 0 are both possible for $z_5$. As displayed in Fig. 9, $z_5$ is located in the vicinity of the tangency point (intersection point), and thus $z_6$ is located in $V_1 \cap H_0$ or $V_1 \cap H_1$ in the vicinity of $\gamma_s$. Hence the symbol for $z_6$ is 1. In the left (resp., right) panel of Fig. 9, the periodic orbit from $z_0$ to $z_8$ with the symbol sequence 011011100 (resp., 011010100) is displayed, where $z_5$ is located in the region $V_1$ (resp., $V_0$). By reversibility, the symbol sequences from $z_9$ to $z_{16}$ are 01110110 and 01010110.

We now explain how to find the general expressions for the periodic orbits appearing in Table I(a). If $z_0$ is located in $L_2$ and $z_9$ in $M_2$, $z_1$ is located slightly above the initial point of the periodic orbit with period $q = 17$. Therefore, we place $s(1,2)$ between two 0's and obtain the symbol sequence for the $(2,2)$-element as 0011011100011101100. Next we consider the periodic orbit with $z_0$ located in $L_1$ and $z_9$ located in $M_3$. We know that $M_3$ is located near $P$. Then, comparing $T^2M_3$, $TM_2$ and $L_1$, it is found that the symbol for $z_{10}$ is 0. Thus the symbol for $z_8$ is also 0. There are three zeros in the middle of $s(1,2)$. Adding two zeros in the middle of $s(1,2)$, we obtain $s(1,3)$ as 0110111000001110110. Repeating these procedures, the two expressions in Eq. (31) are derived.

In order to form the symbol sequences for the orbits appearing in Table II(b),

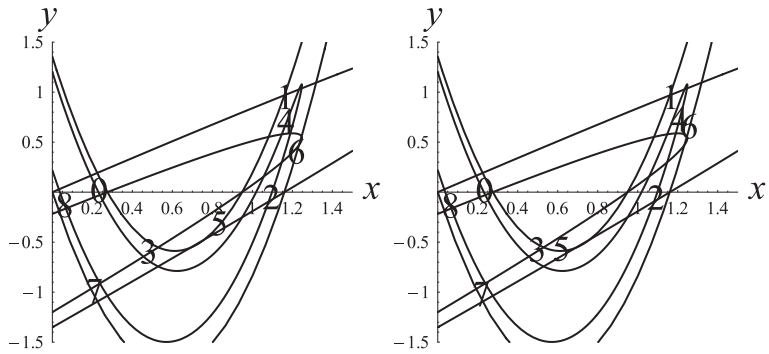


Fig. 9. The orbit from $z_0$ to $z_8$. Here, 0, 1, etc., represent $z_0$, $z_1$, etc. Displayed are two orbits for the $(1, 2)$-element in Table II(a), where $z_2$ is located in the region $V_1$. The symbol sequences are 011011100 for the left orbit and 011010100 for the right orbit.

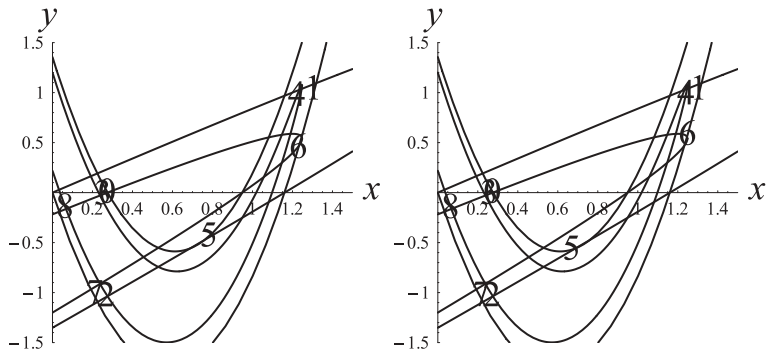


Fig. 10. The orbit from $z_0$ to $z_8$. Displayed are two orbits for the $(1, 2)$-element in Table II(b), where $z_2$ is located in the region $V_0$. The symbol sequences are 010011100 for the left orbit and 010010100 for the right orbit.

we plot the orbital points of the periodic orbit for the $(1, 2)$-element in Table II(b) (see Fig. 10). The difference between Figs. 9 and 10 is only the position of $z_2$. In Fig. 10, it is located in the region $V_0$. Thus, two expressions given in Eq. (32) are obtained.

### 4.3. *The second stage*

The trellis for the second stage at which $T^{-2}\gamma_s$ is tangent to $T^3\Gamma_u$ is illustrated in Fig. 11. The compatible graph is displayed in the lower panel. From the compatible graph, the matrix $M_2$ representing the transitions among $A, B, \cdots, I$ is determined:

$$M_2 = \left(\begin{array}{c|ccccccccc} & B & C & D & E & G & H & F & A & I \\ \hline B & 0 & 0 & 0 & 0 & 0 & 0 & 0 & 1 & 0 \\ C & 0 & 1 & 0 & 1 & 2 & 1 & 2 & 0 & 2 \\ D & 1 & 0 & 0 & 0 & 0 & 0 & 0 & 0 & 0 \\ E & 0 & 1 & 1 & 0 & 0 & 0 & 0 & 0 & 0 \\ G & 0 & 0 & 1 & 0 & 0 & 0 & 0 & 0 & 0 \\ F & 0 & 0 & 1 & 1 & 0 & 1 & 0 & 0 & 0 \\ H & 0 & 0 & 0 & 0 & 1 & 0 & 0 & 0 & 0 \\ A & 0 & 0 & 0 & 0 & 0 & 1 & 0 & 1 & 0 \\ I & 0 & 0 & 0 & 0 & 0 & 0 & 1 & 0 & 0 \end{array}\right). \tag{33}$$

The characteristic equation for $M_2$ is obtained as follows:

$$\lambda^9 - 2\lambda^8 + 2\lambda^3 - 2\sum_{k=0}^{2}\lambda^k = 0. \tag{34}$$

The largest eigenvalue is $\lambda_{\max} = 1.9923$. This value is equal to that of the transition matrix constructed by DMS.[17)]

From Theorem 1, we derive the dynamical orderings III(a) and III(b) for the case with $k = 3,\ k' = 2$ and $i_c = 1$ and the symbol sequences for the periodic orbits appearing in III(a) and III(b).

$$s^2_{\mathrm{III(a)}}(i,j) = \begin{cases} 0^i(1100111)0^{2j-1}(1110011)0^i, \\ 0^i(1100101)0^{2j-1}(1010011)0^i, \end{cases} \tag{35}$$

$$s^2_{\mathrm{III(b)}}(i,j) = \begin{cases} 0^i(1000111)0^{2j-1}(1110001)0^i, \\ 0^i(1000101)0^{2j-1}(1010001)0^i. \end{cases} \tag{36}$$

It is noted that the tangency point of $T^{-2}\gamma_s$ and $T^3\Gamma_u$ is located in a region much closer to $T^{-1}\Gamma_u$ than that of $T^{-2}\gamma_s$ and $T^2\Gamma_u$. This implies that $z_5$ of the orbit $O(z_0)$ in the (1,2)-element of Table III(a) is located in a region closer to $T^{-1}\Gamma_u$ than that of $z'_4$ of the orbit $O(z'_0)$ in the (1,2)-element of Table II(a). The symbol for $z'_3 = T^{-1}z'_4$ is 0 [see Eq. (35)]. Then $z_4$ is located on the left of $z'_3$, and its symbol is 0. The orbit from $z_0$ to $z_5$ passes a region closer to $P$ than that from $z'_0$ to $z'_4$. Finally, the orbit from $z_0$ to $z_5$ is coded as 010001, which has one more 0 than the sequence for the orbit from $z'_0$ to $z'_4$, 01001. Thus, the symbol sequences are determined as 0110011100011100110 and 0110010100010100110. The derivation for the other sequences is omitted.

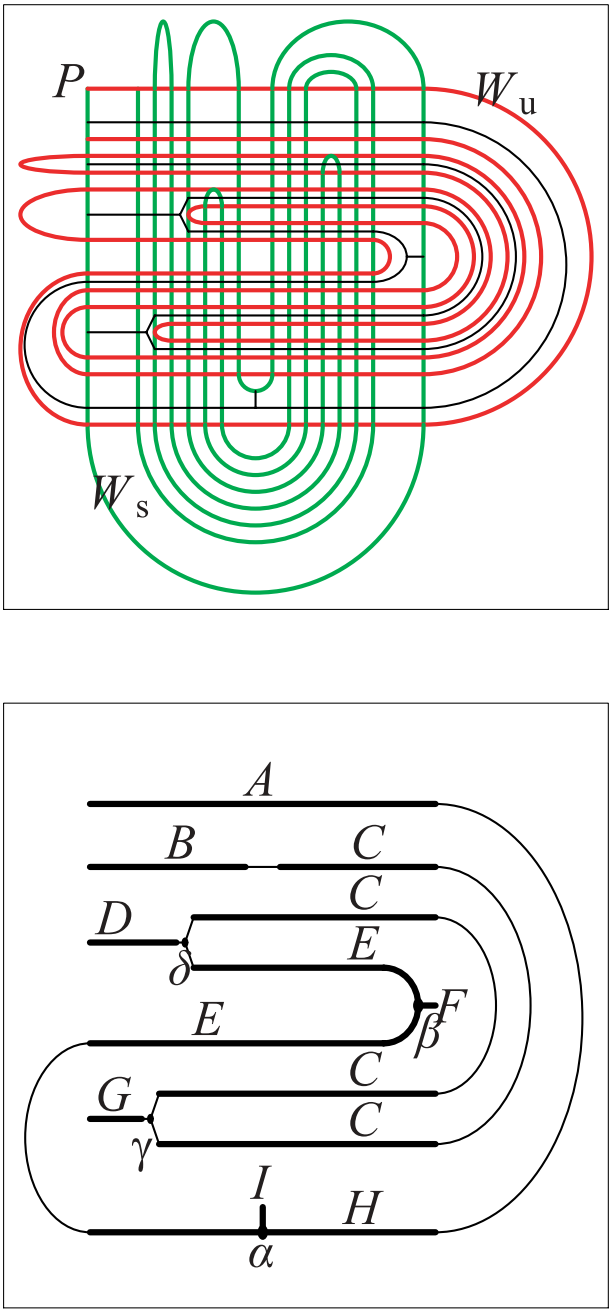


Fig. 11. Trellis (upper panel) for the second stage and its compatible graph $\widehat{\mathcal{G}}$. In the lower panel, the control edges in $\widehat{\mathcal{G}}$ are labeled $A, B, \cdots, I$, and in this case, the relations $\beta = T\alpha$, $\gamma = T\beta$ and $\delta = T\gamma$ hold.

Table III. Dynamical ordering.

(a)

| | $M_2$ | $\Rightarrow$ | $M_3$ | $\Rightarrow$ | $M_4$ | $\Rightarrow$ | $M_5$ | $\Rightarrow \cdots$ |
|---|---|---|---|---|---|---|---|---|
| $L_1$ | 19 | $\leftarrow$ | 21 | $\leftarrow$ | 23 | $\leftarrow$ | 25 | $\leftarrow \cdots$ |
| $\Downarrow$ | $\uparrow$ | | $\uparrow$ | | $\uparrow$ | | $\uparrow$ | |
| $L_2$ | 21 | $\leftarrow$ | 23 | $\leftarrow$ | 25 | $\leftarrow$ | 27 | $\leftarrow \cdots$ |
| $\Downarrow$ | $\uparrow$ | | $\uparrow$ | | $\uparrow$ | | $\uparrow$ | |
| $L_3$ | 23 | $\leftarrow$ | 25 | $\leftarrow$ | 27 | $\leftarrow$ | 29 | $\leftarrow \cdots$ |
| $\Downarrow$ | $\uparrow$ | | $\uparrow$ | | $\uparrow$ | | $\uparrow$ | |
| $L_4$ | 25 | $\leftarrow$ | 27 | $\leftarrow$ | 29 | $\leftarrow$ | 31 | $\leftarrow \cdots$ |
| $\Downarrow$ | $\uparrow$ | | $\uparrow$ | | $\uparrow$ | | $\uparrow$ | |
| $\cdots$ | $\cdots$ | | $\cdots$ | | $\cdots$ | | $\cdots$ | |

(b)

| | $M_2$ | $\Rightarrow$ | $M_3$ | $\Rightarrow$ | $M_4$ | $\Rightarrow$ | $M_5$ | $\Rightarrow \cdots$ |
|---|---|---|---|---|---|---|---|---|
| $L_1$ | 19 | $\leftarrow$ | 21 | $\leftarrow$ | 23 | $\leftarrow$ | 25 | $\leftarrow \cdots$ |
| $\Downarrow$ | $\downarrow$ | | $\downarrow$ | | $\downarrow$ | | $\downarrow$ | |
| $L_2$ | 21 | $\leftarrow$ | 23 | $\leftarrow$ | 25 | $\leftarrow$ | 27 | $\leftarrow \cdots$ |
| $\Downarrow$ | $\downarrow$ | | $\downarrow$ | | $\downarrow$ | | $\downarrow$ | |
| $L_3$ | 23 | $\leftarrow$ | 25 | $\leftarrow$ | 27 | $\leftarrow$ | 29 | $\leftarrow \cdots$ |
| $\Downarrow$ | $\downarrow$ | | $\downarrow$ | | $\downarrow$ | | $\downarrow$ | |
| $L_4$ | 25 | $\leftarrow$ | 27 | $\leftarrow$ | 29 | $\leftarrow$ | 31 | $\leftarrow \cdots$ |
| $\Downarrow$ | $\downarrow$ | | $\downarrow$ | | $\downarrow$ | | $\downarrow$ | |
| $\cdots$ | $\cdots$ | | $\cdots$ | | $\cdots$ | | $\cdots$ | |

### 4.4. *The third stage*

In Fig. 12, we display the trellis for the third stage and its compatible graph. The transition matrix $M_3$ and its characteristic equation are obtained as:

$$M_3 = \left(\begin{array}{c|cccccccccc} & B & C & D & E & F & G & I & J & H & A & K \\ \hline B & 0 & 0 & 0 & 0 & 0 & 0 & 0 & 0 & 0 & 1 & 0 \\ C & 0 & 1 & 0 & 1 & 2 & 1 & 2 & 1 & 2 & 0 & 2 \\ D & 1 & 0 & 0 & 0 & 0 & 0 & 0 & 0 & 0 & 0 & 0 \\ E & 0 & 1 & 1 & 0 & 0 & 0 & 0 & 0 & 0 & 0 & 0 \\ F & 0 & 0 & 1 & 0 & 0 & 0 & 0 & 0 & 0 & 0 & 0 \\ G & 0 & 0 & 1 & 1 & 0 & 1 & 0 & 0 & 0 & 0 & 0 \\ I & 0 & 0 & 0 & 0 & 1 & 0 & 0 & 0 & 0 & 0 & 0 \\ J & 0 & 0 & 0 & 0 & 0 & 1 & 0 & 0 & 0 & 0 & 0 \\ H & 0 & 0 & 0 & 0 & 0 & 0 & 1 & 0 & 0 & 0 & 0 \\ A & 0 & 0 & 0 & 0 & 0 & 0 & 0 & 1 & 0 & 1 & 0 \\ K & 0 & 0 & 0 & 0 & 0 & 0 & 0 & 0 & 1 & 0 & 0 \end{array}\right), \tag{37}$$

and

$$\lambda^{11} - 2\lambda^{10} + 2\lambda^4 - 2\sum_{k=0}^{3} \lambda^k = 0. \tag{38}$$

The largest eigenvalue is $\lambda_{\max} = 1.99808$.

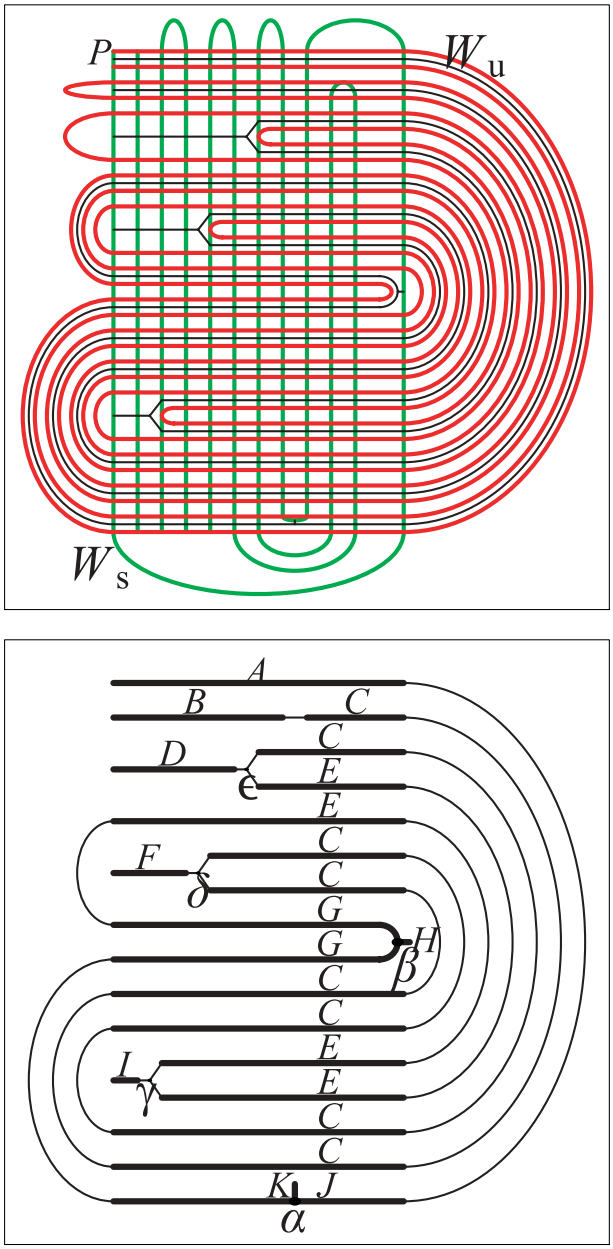


Fig. 12. Trellis (upper graph) for the third stage and its compatible graph $\widehat{\mathcal{G}}$. In the lower graph, the control edges in $\widehat{\mathcal{G}}$ are labeled $A, B, \cdots, K$, and in this case, the relations $\beta = T\alpha$, $\gamma = T\beta$, $\delta = T\gamma$ and $\epsilon = T\delta$ hold.

Table IV. Dynamical ordering.

(a)

| | $M_2$ | $\Rightarrow$ | $M_3$ | $\Rightarrow$ | $M_4$ | $\Rightarrow$ | $M_5$ | $\Rightarrow\cdots$ |
|---|---|---|---|---|---|---|---|---|
| $L_1$ | 21 | $\leftarrow$ | 23 | $\leftarrow$ | 25 | $\leftarrow$ | 27 | $\leftarrow\cdots$ |
| $\Downarrow$ | $\uparrow$ | | $\uparrow$ | | $\uparrow$ | | $\uparrow$ | |
| $L_2$ | 23 | $\leftarrow$ | 25 | $\leftarrow$ | 27 | $\leftarrow$ | 29 | $\leftarrow\cdots$ |
| $\Downarrow$ | $\uparrow$ | | $\uparrow$ | | $\uparrow$ | | $\uparrow$ | |
| $L_3$ | 25 | $\leftarrow$ | 27 | $\leftarrow$ | 29 | $\leftarrow$ | 31 | $\leftarrow\cdots$ |
| $\Downarrow$ | $\uparrow$ | | $\uparrow$ | | $\uparrow$ | | $\uparrow$ | |
| $L_4$ | 27 | $\leftarrow$ | 29 | $\leftarrow$ | 31 | $\leftarrow$ | 33 | $\leftarrow\cdots$ |
| $\Downarrow$ | $\uparrow$ | | $\uparrow$ | | $\uparrow$ | | $\uparrow$ | |
| $\cdots$ | $\cdots$ | | $\cdots$ | | $\cdots$ | | $\cdots$ | |

(b)

| | $M_2$ | $\Rightarrow$ | $M_3$ | $\Rightarrow$ | $M_4$ | $\Rightarrow$ | $M_5$ | $\Rightarrow\cdots$ |
|---|---|---|---|---|---|---|---|---|
| $L_1$ | 21 | $\leftarrow$ | 23 | $\leftarrow$ | 25 | $\leftarrow$ | 27 | $\leftarrow\cdots$ |
| $\Downarrow$ | $\downarrow$ | | $\downarrow$ | | $\downarrow$ | | $\downarrow$ | |
| $L_2$ | 23 | $\leftarrow$ | 25 | $\leftarrow$ | 27 | $\leftarrow$ | 29 | $\leftarrow\cdots$ |
| $\Downarrow$ | $\downarrow$ | | $\downarrow$ | | $\downarrow$ | | $\downarrow$ | |
| $L_3$ | 25 | $\leftarrow$ | 27 | $\leftarrow$ | 29 | $\leftarrow$ | 31 | $\leftarrow\cdots$ |
| $\Downarrow$ | $\downarrow$ | | $\downarrow$ | | $\downarrow$ | | $\downarrow$ | |
| $L_4$ | 27 | $\leftarrow$ | 29 | $\leftarrow$ | 31 | $\leftarrow$ | 33 | $\leftarrow\cdots$ |
| $\Downarrow$ | $\downarrow$ | | $\downarrow$ | | $\downarrow$ | | $\downarrow$ | |
| $\cdots$ | $\cdots$ | | $\cdots$ | | $\cdots$ | | $\cdots$ | |

From Theorem 1, we derive the dynamical orderings IV(a) and (b) for this case with $k = 4$, $k' = 2$ and $i_c = 1$ and the symbol sequences for the periodic orbits appearing in IV(a) and (b).

$$s^3_{\mathrm{IV(a)}}(i,j) = \begin{cases} 0^i(11000111)0^{2j-1}(11100011)0^i, \\ 0^i(11000101)0^{2j-1}(10100011)0^i, \end{cases} \tag{39}$$

$$s^3_{\mathrm{IV(b)}}(i,j) = \begin{cases} 0^i(10000111)0^{2j-1}(11100001)0^i, \\ 0^i(10000101)0^{2j-1}(10100001)0^i. \end{cases} \tag{40}$$

### 4.5. *The n-th stage*

We can similarly derive the transition matrix $M_n$, which we do not give explicitly here. The characteristic equation for $M_n$ is obtained as

$$\lambda^{2n+5} - 2\lambda^{2n+4} + 2\lambda^{n+1} - 2\sum_{k=0}^{n} \lambda^k = 0. \tag{41}$$

From Eq. (41), we can determine the largest eigenvalue $\lambda_{\max}$. For a large value of $n$, we have the topological entropy $h_{\mathrm{top}} = \ln \lambda_{\max} \simeq \ln 2 - 1/(4(2^n + 4^{n+1}))$.

From Theorem 1, we derive the dynamical ordering for this case with $k = n + 1$, $k' = 2$ and $i_c = 1$ and obtain the symbol sequences.

Table V. Dynamical ordering.

(a)-$n$

| | $M_2$ | $\Rightarrow$ | $M_3$ | $\Rightarrow$ | $M_4$ | $\Rightarrow$ | $M_5$ | $\Rightarrow\cdots$ |
|---|---|---|---|---|---|---|---|---|
| $L_1$ | $2n+15$ | $\leftarrow$ | $2n+17$ | $\leftarrow$ | $2n+19$ | $\leftarrow$ | $2n+21$ | $\leftarrow\cdots$ |
| $\Downarrow$ | $\uparrow$ | | $\uparrow$ | | $\uparrow$ | | $\uparrow$ | |
| $L_2$ | $2n+17$ | $\leftarrow$ | $2n+19$ | $\leftarrow$ | $2n+21$ | $\leftarrow$ | $2n+23$ | $\leftarrow\cdots$ |
| $\Downarrow$ | $\uparrow$ | | $\uparrow$ | | $\uparrow$ | | $\uparrow$ | |
| $L_3$ | $2n+19$ | $\leftarrow$ | $2n+21$ | $\leftarrow$ | $2n+23$ | $\leftarrow$ | $2n+25$ | $\leftarrow\cdots$ |
| $\Downarrow$ | $\uparrow$ | | $\uparrow$ | | $\uparrow$ | | $\uparrow$ | |
| $L_4$ | $2n+21$ | $\leftarrow$ | $2n+23$ | $\leftarrow$ | $2n+25$ | $\leftarrow$ | $2n+27$ | $\leftarrow\cdots$ |
| $\Downarrow$ | $\uparrow$ | | $\uparrow$ | | $\uparrow$ | | $\uparrow$ | |
| $\cdots$ | $\cdots$ | | $\cdots$ | | $\cdots$ | | $\cdots$ | |

(b)-$n$

| | $M_2$ | $\Rightarrow$ | $M_3$ | $\Rightarrow$ | $M_4$ | $\Rightarrow$ | $M_5$ | $\Rightarrow\cdots$ |
|---|---|---|---|---|---|---|---|---|
| $L_1$ | $2n+15$ | $\leftarrow$ | $2n+17$ | $\leftarrow$ | $2n+19$ | $\leftarrow$ | $2n+21$ | $\leftarrow\cdots$ |
| $\Downarrow$ | $\downarrow$ | | $\downarrow$ | | $\downarrow$ | | $\downarrow$ | |
| $L_2$ | $2n+17$ | $\leftarrow$ | $2n+19$ | $\leftarrow$ | $2n+21$ | $\leftarrow$ | $2n+23$ | $\leftarrow\cdots$ |
| $\Downarrow$ | $\downarrow$ | | $\downarrow$ | | $\downarrow$ | | $\downarrow$ | |
| $L_3$ | $2n+19$ | $\leftarrow$ | $2n+21$ | $\leftarrow$ | $2n+23$ | $\leftarrow$ | $2n+25$ | $\leftarrow\cdots$ |
| $\Downarrow$ | $\downarrow$ | | $\downarrow$ | | $\downarrow$ | | $\downarrow$ | |
| $L_4$ | $2n+21$ | $\leftarrow$ | $2n+23$ | $\leftarrow$ | $2n+25$ | $\leftarrow$ | $2n+27$ | $\leftarrow\cdots$ |
| $\Downarrow$ | $\downarrow$ | | $\downarrow$ | | $\downarrow$ | | $\downarrow$ | |
| $\cdots$ | $\cdots$ | | $\cdots$ | | $\cdots$ | | $\cdots$ | |

$$s^n_{\mathrm{V.(a)}}(i,j)=\begin{cases}0^i(110^n111)0^{2j-1}(1110^n11)0^i,\\ 0^i(110^n101)0^{2j-1}(1010^n11)0^i,\end{cases} \tag{42}$$

$$s^n_{\mathrm{V(b)}}(i,j)=\begin{cases}0^i(100^n111)0^{2j-1}(1110^n01)0^i,\\ 0^i(100^n101)0^{2j-1}(1010^n01)0^i.\end{cases} \tag{43}$$

### 4.6. *Topological entropy evaluated by the DOM*

Using the symbol sequences and the software *Wintrain*, developed by Hall, the largest rate of increase of the number of periodic orbits is obtained. We call this value $\hat{\lambda}_{\max}$.

We are particularly interested in $\hat{\lambda}_{\max}$ for the $(i,i+1)$-element in both Tables V(a)-$n$ and (b)-$n$. The limit $i\to\infty$ corresponds to the tangency of $T^{n+1}\Gamma_u$ and $T^{-2}\gamma_s$. In Table VI, the values of $\hat{\lambda}_{max}$ obtained using *Wintrain* are listed. Note that the limits of the values in the columns for V(a)-$n$ and V(b)-$n$ are the same for each $n$. Thus, $h_{\mathrm{top}}$ is constant in the $n$-th stage. The accumulation points for both columns are $\lambda_{\max}$, as derived using the trellis method.

### 4.7. *The case in which only Type I dynamical ordering holds*

As remarked in §3.2, the situation with $k=0$, $k'=1$ and $i_c=1$ has only the dynamical ordering of Type I appearing in Table VII.

Table VI. Largest eigenvalue.

| $i$ | V(a)-1 | V(b)-1 | V(a)-2 | V(b)-2 | V(a)-3 | V(b)-3 | V(a)-4 | V(b)-4 |
|---|---|---|---|---|---|---|---|---|
| 1 | 1.859 | 1.867 | 1.882 | 1.882 | 1.9238 | 1.9403 | 1.9606 | 1.9698 |
| 2 | 1.944 | 1.946 | 1.968 | 1.969 | 1.9738 | 1.9739 | 1.9747 | 1.9672 |
| 3 | 1.962 | 1.963 | 1.986 | 1.986 | 1.9923 | 1.9923 | 1.9936 | 1.9936 |
| 4 | 1.967 | 1.967 | 1.990 | 1.990 | 1.9966 | 1.9966 | 1.9980 | 1.9980 |
| 5 | 1.968 | 1.968 | 1.992 | 1.992 | 1.9977 | 1.9977 | 1.9991 | 1.9991 |
| $\lambda_{\max}$ | 1.968 | 1.968 | 1.992 | 1.992 | 1.9980 | 1.9980 | 1.9995 | 1.9995 |

The numbers 1–4 in V(a)-1–V(a)-4 and V(b)-1–V(b)-4 represent the values of $n$.

Table VII. Dynamical ordering.

| | $M_2$ | $\Rightarrow$ | $M_3$ | $\Rightarrow$ | $M_4$ | $\Rightarrow$ | $M_5$ | $\Rightarrow \cdots$ |
|---|---|---|---|---|---|---|---|---|
| $L_1$ | 11 | $\leftarrow$ | 13 | $\leftarrow$ | 15 | $\leftarrow$ | 17 | $\leftarrow \cdots$ |
| $\Downarrow$ | $\uparrow$ | | $\uparrow$ | | $\uparrow$ | | $\uparrow$ | |
| $L_2$ | 13 | $\leftarrow$ | 15 | $\leftarrow$ | 17 | $\leftarrow$ | 19 | $\leftarrow \cdots$ |
| $\Downarrow$ | $\uparrow$ | | $\uparrow$ | | $\uparrow$ | | $\uparrow$ | |
| $L_3$ | 15 | $\leftarrow$ | 17 | $\leftarrow$ | 19 | $\leftarrow$ | 21 | $\leftarrow \cdots$ |
| $\Downarrow$ | $\uparrow$ | | $\uparrow$ | | $\uparrow$ | | $\uparrow$ | |
| $L_4$ | 17 | $\leftarrow$ | 19 | $\leftarrow$ | 21 | $\leftarrow$ | 23 | $\leftarrow \cdots$ |
| $\Downarrow$ | $\uparrow$ | | $\uparrow$ | | $\uparrow$ | | $\uparrow$ | |
| $\cdots$ | $\cdots$ | | $\cdots$ | | $\cdots$ | | $\cdots$ | |

Table VIII. Largest eigenvalue.

| $i$ | VII |
|---|---|
| 1 | 1.874 |
| 2 | 1.974 |
| 3 | 1.993 |
| 4 | 1.998 |
| 5 | 1.999 |
| $\lambda_{\max}$ | 2 |

The symbol sequences for the periodic orbits in Table VII are

$$s_{\mathrm{VII}}(i,j) = \begin{cases} 0^i(101)0^{2j-1}(101)0^i, \\ 0^i(111)0^{2j-1}(111)0^i, \end{cases} \tag{44}$$

where $i \geq 1$ and $j \geq 2$. We list in Table VIII the largest eigenvalues $\hat{\lambda}_{\max}$ for the elements $(i, i+1)$, with $i = 1, 2, 3, 4$ and 5, and their limiting value, $\ln 2$, in the limit $i \to \infty$.

## §5. The largest plateau and its family

Here we consider the tangency of $T^n\Gamma_u$ and $T^{-n}\gamma_s$ on $S_{11}$. The geometry for the case $n = 1$ and the compatible graph are illustrated in Fig. 13. The transition matrix is derived as follows:[8)]

$$M_1 = \left(\begin{array}{c|ccc} & A & B & C \\ \hline A & 1 & 2 & 0 \\ B & 0 & 0 & 1 \\ C & 1 & 0 & 0 \end{array}\right). \tag{45}$$

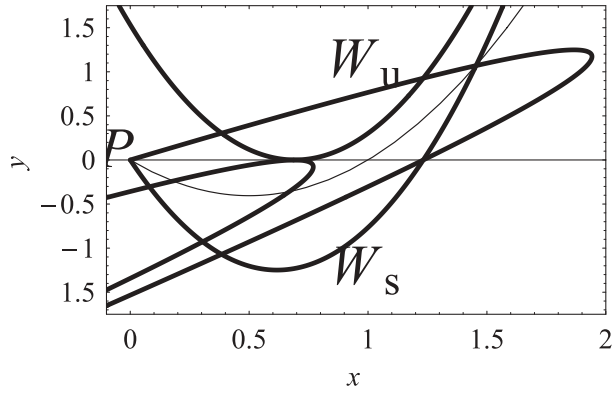


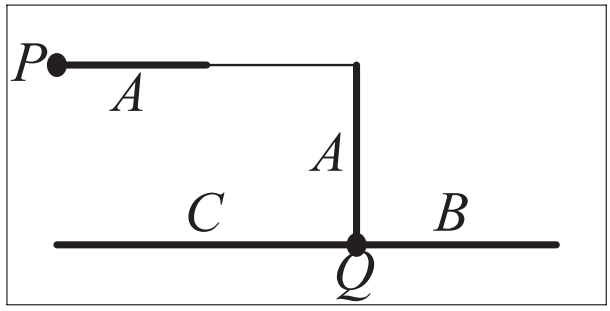


Fig. 13. The upper figure depicts the tangency of $T\Gamma_u$ and $T^{-1}\gamma_s$ at $a = 3.242$, and the lower one shows its compatible graph $\widehat{\mathcal{G}}$, where $A, B$ and $C$ represent the control edges.

Using the same procedure as that used to derive Eq. (45), we have the following $(2n+3) \times (2n+3)$ transition matrix for the tangency of $T^n\Gamma_u$ and $T^{-n}\gamma_s$ on $S_{11}$:

$$M_n = \begin{pmatrix} 1 & 2 & 0 & 0 & \ldots & 0 & 0 & 0 & 0 \\ 0 & 0 & 1 & 0 & \ldots & 0 & 0 & 0 & 0 \\ 0 & 0 & 0 & 1 & \ldots & 0 & 0 & 0 & 0 \\ 0 & 0 & 0 & 0 & \ldots & 0 & 0 & 0 & 0 \\ \ldots & \ldots & \ldots & \ldots & \ldots & \ldots & \ldots & \ldots & \ldots \\ 0 & 0 & 0 & 0 & \ldots & 1 & 0 & 0 & 0 \\ 0 & 0 & 0 & 0 & \ldots & 0 & 1 & 0 & 0 \\ 0 & 0 & 0 & 0 & \ldots & 0 & 0 & 1 & 0 \\ 0 & 0 & 0 & 0 & \ldots & 0 & 0 & 0 & 1 \\ 1 & 0 & 0 & 0 & \ldots & 0 & 0 & 0 & 0 \end{pmatrix}. \tag{46}$$

The characteristic equation is obtained as

$$\lambda^{2n+1} - \lambda^{2n} - 2 = 0. \tag{47}$$

The limit $n \to \infty$ corresponds to the integrable case, $a = 0$. In this limit, $\lambda_{\max}$ tends to 1 and hence $h_{\text{top}}$ tends to zero.

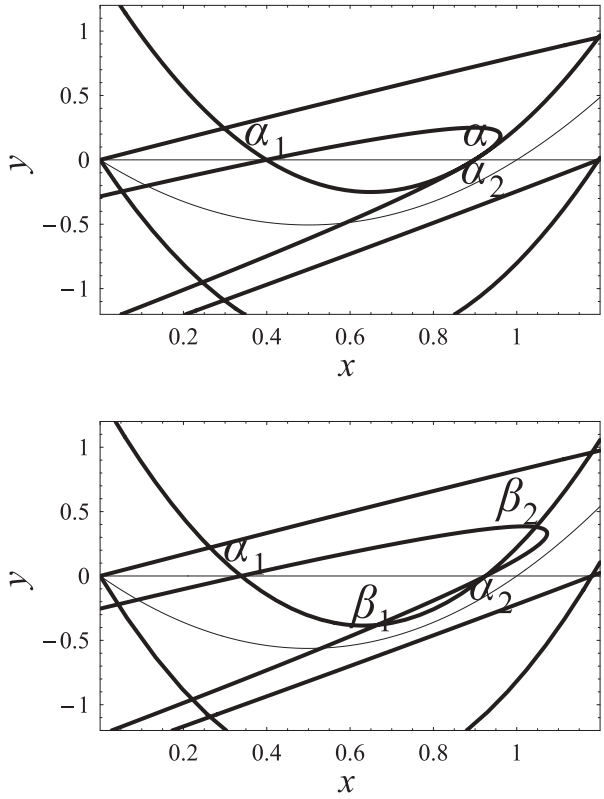


Fig. 14. A bifurcation of the cubic type at the homoclinic point $\alpha_2$ occurs at $a = 4.045$ (upper figure). The lower figure depicts the situation at $a = 4.5$, where the new homoclinic points $\beta_1$ and $\beta_2$ exist.

Here we remark on the first and second instances of tangency of $T\Gamma_u$ and $T\gamma_s$. In the first instance, the tangency is quadratic and in the second it is cubic.[18] The latter situation is displayed in Fig. 14, where the upper panel depicts the cubic tangency situation, and the lower panel shows that the new homoclinic points $\beta_1$ and $\beta_2$ are bifurcated from $\alpha_2$. We call this the cubic-type bifurcation of a homoclinic point.

Because the first tangency of $T\Gamma_u$ and $T^{-1}\gamma_s$ is quadratic, from Theorem 1, the dynamical ordering of Type I with $k = k' = i_c = n(n \geq 1)$ holds. At the second tangency, the dynamical ordering of Type II holds. The results are given in Tables IX(a)-$n$ and IX(b)-$n$.

The symbol sequences for the periodic orbits appearing in Tables IX(a)-$n$ and IX(b)-$n$ are

$$s^n_{\mathrm{IX(a)}}(i,j) = \begin{cases} 0^i(100^{2n-2}01)0^{2j-1}(100^{2n-2}01)0^i, \\ 0^i(100^{2n-2}11)0^{2j-1}(110^{2n-2}01)0^i, \end{cases} \tag{48}$$

$$s^n_{\mathrm{IX(b)}}(i,j) = \begin{cases} 0^i(110^{2n-2}01)0^{2j-1}(100^{2n-2}11)0^i, \\ 0^i(110^{2n-2}11)0^{2j-1}(110^{2n-2}11)0^i, \end{cases} \tag{49}$$

Table IX. Dynamical ordering.

(a)-$n$

| | $M_{n+1}$ | $\Rightarrow$ | $M_{n+2}$ | $\Rightarrow$ | $M_{n+3}$ | $\Rightarrow$ | $M_{n+4}$ | $\Rightarrow \cdots$ |
|---|---|---|---|---|---|---|---|---|
| $L_n$ | $8n+5$ | $\leftarrow$ | $8n+7$ | $\leftarrow$ | $8n+9$ | $\leftarrow$ | $8n+11$ | $\leftarrow \cdots$ |
| $\Downarrow$ | $\uparrow$ | | $\uparrow$ | | $\uparrow$ | | $\uparrow$ | |
| $L_{n+1}$ | $8n+7$ | $\leftarrow$ | $8n+9$ | $\leftarrow$ | $8n+11$ | $\leftarrow$ | $8n+13$ | $\leftarrow \cdots$ |
| $\Downarrow$ | $\uparrow$ | | $\uparrow$ | | $\uparrow$ | | $\uparrow$ | |
| $L_{n+2}$ | $8n+9$ | $\leftarrow$ | $8n+11$ | $\leftarrow$ | $8n+13$ | $\leftarrow$ | $8n+15$ | $\leftarrow \cdots$ |
| $\Downarrow$ | $\uparrow$ | | $\uparrow$ | | $\uparrow$ | | $\uparrow$ | |
| $L_{n+3}$ | $8n+11$ | $\leftarrow$ | $8n+13$ | $\leftarrow$ | $8n+15$ | $\leftarrow$ | $8n+17$ | $\leftarrow \cdots$ |
| $\Downarrow$ | $\uparrow$ | | $\uparrow$ | | $\uparrow$ | | $\uparrow$ | |
| $\cdots$ | $\cdots$ | | $\cdots$ | | $\cdots$ | | $\cdots$ | |

(b)-$n$

| | $M_{n+1}$ | $\Rightarrow$ | $M_{n+2}$ | $\Rightarrow$ | $M_{n+3}$ | $\Rightarrow$ | $M_{n+4}$ | $\Rightarrow \cdots$ |
|---|---|---|---|---|---|---|---|---|
| $L_n$ | $8n+5$ | $\leftarrow$ | $8n+7$ | $\leftarrow$ | $8n+9$ | $\leftarrow$ | $8n+11$ | $\leftarrow \cdots$ |
| $\Downarrow$ | $\downarrow$ | | $\downarrow$ | | $\downarrow$ | | $\downarrow$ | |
| $L_{n+1}$ | $8n+7$ | $\leftarrow$ | $8n+9$ | $\leftarrow$ | $8n+11$ | $\leftarrow$ | $8n+13$ | $\leftarrow \cdots$ |
| $\Downarrow$ | $\downarrow$ | | $\downarrow$ | | $\downarrow$ | | $\downarrow$ | |
| $L_{n+2}$ | $8n+9$ | $\leftarrow$ | $8n+11$ | $\leftarrow$ | $8n+13$ | $\leftarrow$ | $8n+15$ | $\leftarrow \cdots$ |
| $\Downarrow$ | $\downarrow$ | | $\downarrow$ | | $\downarrow$ | | $\downarrow$ | |
| $L_{n+3}$ | $8n+11$ | $\leftarrow$ | $8n+13$ | $\leftarrow$ | $8n+15$ | $\leftarrow$ | $8n+17$ | $\leftarrow \cdots$ |
| $\Downarrow$ | $\downarrow$ | | $\downarrow$ | | $\downarrow$ | | $\downarrow$ | |
| $\cdots$ | $\cdots$ | | $\cdots$ | | $\cdots$ | | $\cdots$ | |

Table X. Largest eigenvalue.

| $i$ | IX(a)-1 | IX(b)-1 | IX(a)-2 | IX(b)-2 | IX(a)-3 | IX(b)-3 | IX(a)-4 | IX(b)-4 |
|---|---|---|---|---|---|---|---|---|
| 1 | 1.427 | 1.495 | | | | | | |
| 2 | 1.634 | 1.637 | 1.251 | 1.288 | | | | |
| 3 | 1.676 | 1.677 | 1.386 | 1.389 | 1.178 | 1.203 | | |
| 4 | 1.689 | 1.689 | 1.424 | 1.425 | 1.279 | 1.281 | 1.138 | 1.157 |
| 5 | 1.693 | 1.693 | 1.439 | 1.439 | 1.312 | 1.312 | 1.219 | 1.220 |
| 6 | 1.694 | 1.694 | 1.445 | 1.445 | 1.327 | 1.327 | 1.248 | 1.248 |
| 7 | 1.695 | 1.695 | 1.447 | 1.447 | 1.334 | 1.334 | 1.261 | 1.261 |
| 8 | 1.695 | 1.695 | 1.449 | 1.449 | 1.337 | 1.337 | 1.269 | 1.269 |
| 9 | | | 1.450 | 1.450 | 1.339 | 1.339 | 1.273 | 1.273 |
| 10 | | | | | 1.340 | 1.340 | 1.275 | 1.275 |
| $\lambda_{\max}$ | 1.695 | 1.695 | 1.451 | 1.451 | 1.342 | 1.342 | 1.279 | 1.279 |

where $i \geq n$, $j \geq n+1$ and $n \geq 1$.

The largest eigenvalues, $\hat{\lambda}_{\max}$, accumulate at $\lambda_{\max}$, which is determined by Eq. (47) (see Table X).

## §6. Concluding remarks

Hagiwara and Shudo[19] constructed a pruning algorithm to evaluate the topological entropy. However, there is no guarantee that this algorithm gives a lower bound or an upper bound of the entropy, though the algorithm is quite complicated. For the Hénon map, we cannot judge whether the concept of pruning is valid.

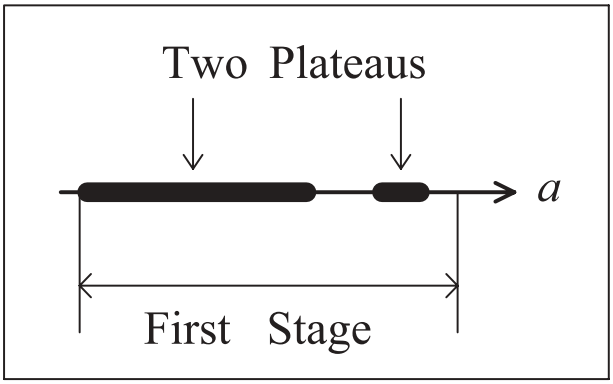


Fig. 15. A schematic depiction of the first stage, for which $a \in [4.975, 5.145]$, and two plateaus, for which $a \in (4.975, 5.113)$ and $(5.124, 5.141)$.

In concluding this paper, let us consider the internal structure of the first stage (§4.2). We need to distinguish two concepts, that of the stage and that of the plateau. In Fig. 15, we depict the first stage, in which two plateaus exist.[17)–19)] The left end of the first plateau coincides with the left end of the first stage, whereas the right end of the second plateau does not coincide with the right end of the first stage. Our results presented in §4.2 show that the symmetric periodic orbits appear through saddle-node bifurcations before and after the end of this stage. Thus the number of the periodic point is not constant in this parameter region. Arai[22)] determined the interval of parameter values in which the plateaus are hyperbolic. The two plateaus approximately coincide with the intervals determined by Arai. Part of the first stage is non-hyperbolic. There may exist small hyperbolic intervals in the first stage between the two plateaus.

From Fig. 15 and the result of Ref. 19), we find that the lower bound of the topological entropy increases after the first plateau and is constant in the second plateau. Our results do not account for this fact. To determine the detailed structure of the topological entropy in the first stage, we need to find the tangency situation that contributes to the complexity.

For the Hénon map, we can apply the Biham-Wenzel method to calculate the number of periodic orbit. Using this result, we can determine the detailed structure in the first stage. However, for other mapping systems, there is no method to evaluate the number of periodic points. Our method and the trellis method are applicable to such systems in order to derive a lower bound of the topological entropy.

Sterling, Dullin and Meiss[18)] studied the cubic-type bifurcation of homoclinic points. As mentioned in §5, the critical value of this bifurcation determines the value of the end of the stage. The ordering of Type II holds before and after this tangency.

**Acknowledgements**

We thank Dr. A. Sannami for helpful comments.

**References**


1) S. E. Newhouse, Topology **13** (1974), 9.
2) G. D. Birkhoff, Acta. Math. **81** (1920), 44.
3) R. de Vogelaere, in *Contributions to the Theory of Oscillations*, Vol. IV, Ann. Math. Studies No. 41 (Princeton University Press, 1958).
4) Y. Yamaguchi and K. Tanikawa, Prog. Theor. Phys. **107** (2002), 1117.
5) Y. Yamaguchi and K. Tanikawa, Prog. Theor. Phys. **113** (2005), 935.
6) P. Boyland, Topology and its Appl. **58** (1994), 223.
7) T. Matsuoka, in *Dynamical System* **1** (World Scientific, 1986), p. 58; Contemp. Math. **152** (1993), 229.
   See also Bussei Kenkyu (Kyoto) **67** (1996), 1.
8) P. Collins, Int. J. Bifurcation and Chaos **12** (2002), 605.
   See also "Dynamics of surface maps with homoclinic and heteroclinic tangles", Ph. D thesis (University of California, Berkeley, 1999).
9) T. Hall, *Wintrain*, Software available from
   `http://www.liv.ac.uk/maths/PURE/MIN_SET/CONTENT/members/T_Hall.html`
10) J. Nielsen, Acta. Math. **50** (1927), 189; ibid. **53** (1929), 1; ibid. **58** (1931), 87.
11) W. P. Thurston, Bull. Amer. Math. Soc. (N.S.) **19** (1988), 417.
12) A. J. Casson and S. A. Bleiler, *Automorphisms of Surface after Nielsen and Thurston* (Cambridge University Press, 1988).
13) M. Bestvina and M. Handel, Ann. of Math. **135** (1992), 1.
14) M. Hénon, Commun. Math. Phys. **50** (1976), 69.
15) O. Biham and W. Wenzel, Phys. Rev. Lett. **63** (1989), 819.
16) O. Biham and W. Wenzel, Phys. Rev. A **42** (1990), 4639.
17) M. J. Davis, R. S. Mackay and A. Sannami, Physica D **52** (1991), 171.
18) D. Sterling, H. R. Dullin and J. D. Meiss, Physica D **134** (1999), 153.
19) R. Hagiwara and A. Shudo, J. of Phys. A **37** (2004), 10521.
20) R. Brown, Ergod. Th. & Dynam. Sys. **15** (1995), 1045.
21) J. Palis, Topology **8** (1969), 385.
22) J. Arai, *On Hyperbolic Plateaus of Henon Maps*, `http://www.math.kyoto-u.ac.jp/~arai/`